

JAERI-M
91-195

IMPROVED DIVERTOR CONFINEMENT OBSERVED
IN JT-60

November 1991

Shunji TSUJI, Nobuyuki HOSOGANE
Kiyoshi ITAMI, Hirotaka KUBO
Takeo NISHITANI, Michiya SHIMADA
Yoshihiko KOIDE, Nobuhiro NISHINO*
Tatsuo SUGIE, Keisuke NAGASHIMA
Yasunori KAWANO, Osamu NAITO
Hiroo NAKAMURA, Hidetoshi YOSHIDA
Naoyuki MIYA and Masayuki NAGAMI

JAERI-M レポートは、日本原子力研究所が不定期に公刊している研究報告書です。
入手の間合わせは、日本原子力研究所技術情報部情報資料課（〒319-11茨城県那珂郡東海村）
あて、お申しこしください。なお、このほかに財団法人原子力弘済会資料センター（〒319-11茨城
県那珂郡東海村日本原子力研究所内）で複写による実費頒布をおこなっております。

JAERI-M reports are issued irregularly.
Inquiries about availability of the reports should be addressed to Information Division, Department
of Technical Information, Japan Atomic Energy Research Institute, Tokai-mura, Naka-gun,
Ibaraki-ken 319-11, Japan.

© Japan Atomic Energy Research Institute, 1991

編集兼発行	日本原子力研究所
印刷	日立高速印刷株式会社

Improved Divertor Confinement Observed in JT-60

Shunji TSUJI, Nobuyuki HOSOGANE, Kiyoshi ITAMI
Hirotaka KUBO, Takeo NISHITANI, Michiya SHIMADA
Yoshihiko KOIDE, Nobuhiro NISHINO*, Tatsuo SUGIE
Keisuke NAGASHIMA, Yasunori KAWANO, Osamu NAITO
Hiroo NAKAMURA, Hidetoshi YOSHIDA, Naoyuki MIYA
and Masayuki NAGAMI

Department of Fusion Plasma Research
Naka Fusion Research Establishment
Japan Atomic Energy Research Institute
Naka-machi, Naka-gun, Ibaraki-ken

(Received October 15, 1991)

An improved divertor confinement (IDC) regime has been found in the lower X-point configuration of JT-60. Improvement in particle confinement was observed in beam heated hydrogen plasmas when both the heating power and line averaged density exceeded thresholds. The radiation power from the divertor plasma increased to as much as 50% of heating power. Discharges with improvement in energy confinement by up to 20% and enhanced divertor radiation lasted for several seconds in a quasi-steady state without significant impurity accumulation in the core. The threshold line averaged electron density for IDC increased linearly with power and dropped with increasing safety factor. The in-out asymmetry of particle recycling changed with B_t direction and the improvements were observed only when ion ∇B drift was toward the X-point. These findings suggest that collisional transport near the separatrix is connected with the onset of the IDC regime.

Keywords: Tokamak, Divertor, JT-60, Improved Divertor Confinement, Energy Confinement, Particle Confinement, H mode, Remote Radiative Cooling, Collisional Transport

* Energy Research Laboratory, Hitachi Ltd

J T-60において観測された改善ダイバータ閉じ込め

日本原子力研究所那珂研究所炉心プラズマ研究部

辻 俊二・細金 延幸・伊丹 潔
久保 博孝・西谷 健夫・嶋田 道也
小出 芳彦・西野 信博*・杉江 達夫
永島 圭介・河野 康則・内藤 磨
中村 博雄・吉田 英俊・宮 直之
永見 正幸

(1991年10月15日受理)

改善ダイバータ閉じ込め (IDC) と呼ぶ現象が、J T-60の下X点配位で観測された。すなわち、ダイバータ部での放射パワーが加熱入力50%にも達する遠隔放射冷却が実現し、かつエネルギー閉じ込めが20%改善した状態が、主プラズマでの不純物の蓄積を起こすことなく数秒間持続する。IDCとなる電子密度の閾値は、加熱パワーに対してほぼ比例し、安全係数を高めると下がる。トロイダル磁場の向きにより粒子循環のトーラス内外非対称性が変化し、閉じ込めに改善があるのは、イオン ∇B ドリフトがX点に向いているときのみである。これらの観測事実は、セパトリクス付近での衝突効果による粒子束の変化が改善ダイバータ閉じ込めの発生に絡んでいることを示唆している。

Contents

1. Introduction	1
2. Experimental Arrangement	3
3. Bt Reversal Experiments	5
4. Characteristics of IDC	8
4.1 Onset Condition for IDC	8
4.2 Time Evolution of IDC	10
4.3 Global Power Balance	13
4.4 Energy Confinement Improvement by IDC	14
5. Discussion	17
6. Summary	24
Acknowledgements	25
References	26
Appendix A Evaluation of Change in Particle Confinement from Electron Line Density and Neutral Pressure around the Main Plasma	45
Appendix B Estimation of Divertor Ionization from Divertor H_{α} Emission and Neutral Pressure around the Main Plasma	46

目 次

1. 序論	1
2. 実験装置	3
3. Bt 反転実験	5
4. IDC の特性	8
4.1 IDC の発生条件	8
4.2 IDC の時間発展	10
4.3 グローバルなパワー収支	13
4.4 IDC によるエネルギー閉じ込め改善	14
5. 議論	17
6. まとめ	24
謝 辞	25
参考文献	26
付録A 電子密度と中性ガス圧に基づく粒子閉じ込め変化の評価	45
付録B H_{α} 線強度と中性ガス圧からのダイバータ部イオン化率の見積り	46

1. INTRODUCTION

Steady-state operation with enhanced confinement is required to achieve ignition and long-pulse burn in the next generation of tokamaks such as ITER. Reduction of the heat flux onto divertor plates is a crucial issue to secure the steady burn operation. Formation of cold and dense divertor plasmas [1,2] by remote radiative cooling [3-5] is indispensable to alleviate heat load on the divertor plates and to lessen particle pumping requirement.

An improved divertor confinement (IDC) regime has been observed in the lower X-point configuration of JT-60 [6-9] with the following characteristics: the particle confinement improves in a quasi-steady state for several seconds; remote radiative cooling develops in the divertor region with radiated powers of up to 10 MW, which corresponds to 50% of the input power. The energy confinement time was improved by up to 20%. Asymmetric particle recycling and radiation power were observed between inner and outer divertor separatrices. Carbon emission is highest at the inner separatrix, and hence the reduction in the heat load onto the inner divertor plates was significant. This situation is advantageous for next-step tokamaks because the limited space of the inner divertor region makes it difficult to install divertor plates at an angle nearly tangential to the magnetic field lines which is needed to decrease the net heat flux. Although we had previously reported that the particle recycling in the divertor was very high in the IDC regime [6,7], we have now found that divertor particle recycling does not enhance appreciably during IDC. The previous result was due to contamination of H_{α} (656.3 nm) signals

(through interference filters with FWHM of about 4.5 nm) by C II line (657.8 nm) emission [10].

We operated JT-60 in four combinations of I_p and B_t polarities to examine the effects of ion ∇B drift ($B \times \nabla B$) direction on IDC and to check the symmetry of the device. As a result, we found that the IDC regime developed only when the ion ∇B drift was toward the X-point. Reversal of B_t direction changed particle confinement and light impurity behavior significantly. A reduction in oxygen impurities was observed when the ion ∇B drift was toward the X-point and the heating power exceeded a threshold power of about 9 MW. Reversal of I_p direction did not significantly affect the confinement properties and impurity behavior. The B_t polarity dependence of the particle confinement agrees with Hinton and Staebler's theory on collisional transport near the separatrix [11]. Staebler has extended that theory and has proposed a model of the IDC regime by considering carbon behavior and collisional transport effects at the plasma edge [12].

Pronounced vertical asymmetry in the impurity radiation has been observed in limiter discharges. The sign of the asymmetry was opposite to the ion ∇B drift direction in Alcator [13] and PDX [14]. However, in PLT the vertical asymmetry in impurity density was found to be correlated with details of the gas feed, the positioning of the limiter and the plasma temperature near the limiter edge [15]. In JT-60, the divertor radiation was highest when the ion ∇B drift was toward the X-point.

The magnetic configuration and diagnostics used in this study are depicted in Section 2. Changes in particle recycling and impurity shielding effects are described in Section 3. Section 4 presents a characterization of the IDC regime such as onset conditions, parameter

dependences of the divertor radiation and the global energy confinement. Section 5 is devoted to discussion. A summary is given in Section 6.

2. EXPERIMENTAL ARRANGEMENT

A cross-sectional view of a typical lower X-point configuration of JT-60 is shown in Fig. 1 together with diagnostic viewing chords and locations of measurements. The major and averaged minor radii of the plasma were about 3.1 m and 0.7 m, respectively. The plasma elongation was about 1.4. The height of the X-point from divertor plates was normally 3 ~ 5 cm. The gap between the plasma edge and outer limiters is larger than 10 cm. The limiter and divertor plate material was graphite. The working gas was hydrogen. The gas was puffed from outer ports so that the flow reversal effect by gas fueling is unlikely to be effective. Neutral hydrogen beams at around 65 keV were injected with powers up to 25 MW. The experiments were conducted at an average wall temperature of about 280°C. No special wall conditioning was employed for getting IDC except Taylor-type discharge cleaning after vacuum opening.

Diagnostics mainly of particles and impurity line emissions are respectively illustrated in Fig. 1(a) and (b). The fields of view for line emissions are indicated by pairs of solid lines. The line integral of electron density was measured by 2 FIR interferometers along off-axis vertical chords ($\bar{n}_e|_{U6}$ and $\bar{n}_e|_{U23}$) and by a 2-mm μ -wave interferometer along an oblique chord which passes near the magnetic axis of the plasma ($\bar{n}_e|_{IN2}$). The 2-mm interferometer signal, however, often suffered from fringe losses. Hence the line averaged electron

dependences of the divertor radiation and the global energy confinement. Section 5 is devoted to discussion. A summary is given in Section 6.

2. EXPERIMENTAL ARRANGEMENT

A cross-sectional view of a typical lower X-point configuration of JT-60 is shown in Fig. 1 together with diagnostic viewing chords and locations of measurements. The major and averaged minor radii of the plasma were about 3.1 m and 0.7 m, respectively. The plasma elongation was about 1.4. The height of the X-point from divertor plates was normally 3 ~ 5 cm. The gap between the plasma edge and outer limiters is larger than 10 cm. The limiter and divertor plate material was graphite. The working gas was hydrogen. The gas was puffed from outer ports so that the flow reversal effect by gas fueling is unlikely to be effective. Neutral hydrogen beams at around 65 keV were injected with powers up to 25 MW. The experiments were conducted at an average wall temperature of about 280°C. No special wall conditioning was employed for getting IDC except Taylor-type discharge cleaning after vacuum opening.

Diagnostics mainly of particles and impurity line emissions are respectively illustrated in Fig. 1(a) and (b). The fields of view for line emissions are indicated by pairs of solid lines. The line integral of electron density was measured by 2 FIR interferometers along off-axis vertical chords ($\bar{n}_e|_{U6}$ and $\bar{n}_e|_{U23}$) and by a 2-mm μ -wave interferometer along an oblique chord which passes near the magnetic axis of the plasma ($\bar{n}_e|_{IN2}$). The 2-mm interferometer signal, however, often suffered from fringe losses. Hence the line averaged electron

density used in this study was estimated chiefly by the FIR measurement along the outer vertical chord (U6) with an experimentally determined multiplier of 1.4. The measurement points of the 8-channel Thomson scattering using an off-axis laser beam are shown by closed circles. The spatial resolutions were about 4 cm for the outermost 3 channels and 9 ~ 13 cm for the inner channels. Typical estimated errors were about $\pm 2 \times 10^{18} \text{ m}^{-3}$ for electron density and $\pm 10\%$ for electron temperature. Neutral particle pressures were measured at three locations; outside of torus just above the midplane by an ion gauge, lower outside by a Penning gauge and near the inner separatrix of the divertor by a residual gas analyzer (RGA). The H_α emission from the main plasma was monitored by 4 channels of oblique chords (H_α^{MAIN}) and 3 channels of vertical chords (H_α^{U}). Distribution of H_α emission at the divertor plates was viewed by a TV camera with an interference filter. The surface temperature of the plates was recorded by an infrared TV camera with the same viewing field [16]. The spatial resolution was about 9 mm and temperature resolution was about 5°C . The radiation power loss from the divertor region was measured by a bolometer along a horizontal chord ($P_{\text{RAD}}^{\text{DIV}}$). The radiation power loss from the main plasma was monitored by two 15-channel bolometer arrays (schematically shown in Fig. 13) whose spatial resolution in minor radius was about 7 cm [10,17,18] .

Impurity line radiations were measured by a multi-chordal vacuum ultra-violet (VUV) spectrometer (0.5 ~ 50 nm) through an upper outside port [19]. Light impurity line emission in the ultra-violet range of 200 ~ 400 nm was measured by a 12-channel mirror-scanned monochromator along lower chords. The impurity line radiation in the divertor region was measured by an absolutely calibrated grazing

incidence spectrometer (1.5~135 nm) along a vertical chord (U4) which views the inner divertor separatrix and a multi-channel visible spectrometer along a horizontal chord, the view field of which is larger than that of the divertor bolometer. The H_{α}^{DIV} signal used in this paper was obtained from this visible spectrometer so that it is free from the CII contamination. This signal includes the whole divertor H_{α} emission while the H_{α}^{U4} signal comes chiefly from the inner leg of the divertor. The intensity of visible bremsstrahlung emission at 523.3 ± 0.5 nm was measured along two chords (IN2 and U6) to evaluate effective ionic charge, Z_{eff} .

3. B_T REVERSAL EXPERIMENTS

Discharge waveforms with nearly the same NB power and line averaged electron density are compared in Fig. 2 to illustrate the distinct time evolution with B_t reversal. The plasma current (1 MA) and toroidal magnetic field (4.5 T) were reversed at the same time to keep the helical magnetic field structure and, in particular, the field lines impinging on the divertor plates the same. A dramatic difference is seen in the neutral particle pressure around the main plasma measured by the Penning gauge ($P_{NEUTRAL}^{MAIN}$). Oxygen impurities in the main plasma represented by the OVIII line (1s-2p 1.897 nm) decreased with time when the ion ∇B drift was toward the X-point (solid traces), while it increased just the same way as the neutral pressure when the ion ∇B drift was away from the X-point (broken traces). Carbon impurities behaved in an opposite fashion as shown by the C VI line (1s-2p 3.374 nm) trace. When the O VIII intensity was reduced, carbon influx from the divertor was enhanced as seen from the C II (657.8 nm) trace. The

incidence spectrometer (1.5~135 nm) along a vertical chord (U4) which views the inner divertor separatrix and a multi-channel visible spectrometer along a horizontal chord, the view field of which is larger than that of the divertor bolometer. The H_{α}^{DIV} signal used in this paper was obtained from this visible spectrometer so that it is free from the CII contamination. This signal includes the whole divertor H_{α} emission while the H_{α}^{U4} signal comes chiefly from the inner leg of the divertor. The intensity of visible bremsstrahlung emission at 523.3 ± 0.5 nm was measured along two chords (IN2 and U6) to evaluate effective ionic charge, Z_{eff} .

3. B_T REVERSAL EXPERIMENTS

Discharge waveforms with nearly the same NB power and line averaged electron density are compared in Fig. 2 to illustrate the distinct time evolution with B_t reversal. The plasma current (1 MA) and toroidal magnetic field (4.5 T) were reversed at the same time to keep the helical magnetic field structure and, in particular, the field lines impinging on the divertor plates the same. A dramatic difference is seen in the neutral particle pressure around the main plasma measured by the Penning gauge ($P_{NEUTRAL}^{MAIN}$). Oxygen impurities in the main plasma represented by the OVIII line (1s-2p 1.897 nm) decreased with time when the ion ∇B drift was toward the X-point (solid traces), while it increased just the same way as the neutral pressure when the ion ∇B drift was away from the X-point (broken traces). Carbon impurities behaved in an opposite fashion as shown by the C VI line (1s-2p 3.374 nm) trace. When the O VIII intensity was reduced, carbon influx from the divertor was enhanced as seen from the C II (657.8 nm) trace. The

IDC regime started around 5 sec in shot E9107 and the plasma stored energy evaluated by a diamagnetic measurement increased by 15%. The plasma stored energy saturated early with reversed B_t (E9154).

The radiation power from the divertor region was well correlated with the C II signal. Note that the radiation power from the main plasma is higher and that the divertor radiation power was suppressed at lower levels with reversed B_t ($B \times \nabla B$ away from the X-point). Heating power dependences of those radiated power fractions are plotted in Fig. 3. During IDC when the heating power exceeded 14 MW, the radiation power from the main plasma was reduced to around 20% of the heating power and the divertor radiation power fraction was enhanced up to 50%. The divertor radiation fraction increased only modestly with power when the ion ∇B drift was away from the X-point (no-IDC). The higher radiation powers from the main plasma with the ion ∇B drift toward the X-point correlate with higher Z_{eff} values as indicated in Fig. 4.

The characteristics of particle recycling are examined in Figs. 5 and 6. There was an in-out asymmetry in the particle recycling around the main plasma. The intensity of H_α emission along the outer vertical chord (U6) is plotted as a function of the line averaged density in Fig. 5(a). It increased more sharply with increasing density when the ion ∇B drift was away from the X-point than with the opposite B_t direction. The difference in the increasing rate was reversed in the case of the H_α intensity along the inner vertical chord (U23). Thus the inner to outer H_α intensity ratio, a measure of the particle recycling asymmetry, behaved oppositely depending on the B_t direction as shown in Fig. 5(b). The particle recycling occurs more frequently at the inner side of torus when the ion ∇B drift was toward the X-point. This tendency was

pronounced with increasing density. Figure 6 shows that both divertor H_{α} emission and neutral pressure around the main plasma increased parabolically with the line-averaged electron density of the main plasma. Those levels, however, were different with B_t polarities. Whereas particle recycling (H_{α}) in the divertor was higher with the ion ∇B drift toward the X-point (before IDC), the neutral pressure was lower around the main plasma. These observations imply that the particle confinement was better and the particle recycling was more localized in the divertor with the ion ∇B drift toward the X-point. The particle confinement was improved further during IDC with relaxed localization of particle recycling since the both strengths were reduced. The parabolic dependence of both the divertor H_{α} emission and the neutral pressure around the main plasma on the line averaged density can be explained by an inversely-linear dependence of the global particle confinement on density [20,21]. As shown in Appendix A, the change in the global particle confinement time can be estimated by $\bar{n}_e^2 / P_{NEUTRAL}$ [22]. Accordingly the particle confinement time is considered to be improved by a factor of 2 ~ 3 in the IDC regime.

If one normalizes the divertor H_{α} emission to the neutral pressure the difference in recycling between the two ion ∇B drift directions is more clearly shown. The IDC data points lie along the same line as the non-IDC data for the same ion ∇B direction as shown in Fig. 7 (a). The ordinate is a measure of hydrogen ionization in the divertor from a zero-dimensional argument described in Appendix B. Thus the divertor effects are concluded to be enhanced with the ion ∇B drift toward the X-point.

The dominant sources of carbon impurities were the divertor plates. The local carbon influx can be evaluated from line radiation

strengths of lower ionized states of carbon ions such as C II [23,24]. The carbon contents in the main plasma have been experimentally confirmed to be proportional to the C VI line strength [19]. Thereby Fig. 7(b) shows that the level of carbon influx from the divertor is separated with B_t directions when it is normalized to the carbon contents in the main plasma. This observation suggests that carbon ions in the main plasma did not increase as much as the carbon influx, i.e., shielding effects on carbon impurities by the divertor were enhanced with the ion ∇B drift toward the X-point. The two closed circles at high electron densities are data from strongly gas-puffed discharges. Consequently the divertor shielding effects might have been lowered by gas puffing.

4. CHARACTERISTICS OF IDC

4.1 Onset condition for IDC

The IDC regime was observed only when the ion ∇B drift was toward the X-point. Although the preferred direction of the ion ∇B drift is common to the H mode, the dependence on B_t was opposite. Thus the H mode and IDC are independent phenomena. The IDC regime was easily obtained at high B_t , whereas the threshold power for the H mode increases with toroidal magnetic field [25,26]. In JT-60, H-mode transitions were observed in low density discharges when B_t was around 3.3 T [7,27]. The IDC regime set in afterwards at higher electron densities at these magnetic fields as an example shot shown in Fig. 8. In this shot, the H mode was triggered at 5.7 sec and thus the plasma stored energy and the electron density rose until they reached

strengths of lower ionized states of carbon ions such as C II [23,24]. The carbon contents in the main plasma have been experimentally confirmed to be proportional to the C VI line strength [19]. Thereby Fig. 7(b) shows that the level of carbon influx from the divertor is separated with B_t directions when it is normalized to the carbon contents in the main plasma. This observation suggests that carbon ions in the main plasma did not increase as much as the carbon influx, i.e., shielding effects on carbon impurities by the divertor were enhanced with the ion ∇B drift toward the X-point. The two closed circles at high electron densities are data from strongly gas-puffed discharges. Consequently the divertor shielding effects might have been lowered by gas puffing.

4. CHARACTERISTICS OF IDC

4.1 Onset condition for IDC

The IDC regime was observed only when the ion ∇B drift was toward the X-point. Although the preferred direction of the ion ∇B drift is common to the H mode, the dependence on B_t was opposite. Thus the H mode and IDC are independent phenomena. The IDC regime was easily obtained at high B_t , whereas the threshold power for the H mode increases with toroidal magnetic field [25,26]. In JT-60, H-mode transitions were observed in low density discharges when B_t was around 3.3 T [7,27]. The IDC regime set in afterwards at higher electron densities at these magnetic fields as an example shot shown in Fig. 8. In this shot, the H mode was triggered at 5.7 sec and thus the plasma stored energy and the electron density rose until they reached

steady state by excitation of edge localized modes (ELMs). They began to increase again around 6.3 sec which indicates further improvements in the energy and particle confinements by IDC. The increment in the plasma stored energy, however, was modest since it evolved from the H-mode phase. IDC did not occur at low fields below 3 T. At higher B_t of around 4 T, IDC started at lower densities from the L mode and ELMs were observed later when the poloidal beta became higher than a limit which increases linearly with the safety factor [28]. Figure 9 summarizes the points where the IDC regime, L/H transitions and ELMs appear in the domain of line averaged electron density and absorbed power. The high B_t discharges are considered to be marginal for H mode since no sharp H transition was detected within applied powers up to 23 MW. The reason why high B_t was favorable for IDC is that there were q -dependences of the threshold density, energy confinement and remote radiative cooling.

Figure 10 shows that there were thresholds both for the electron density and for the absorbed power with respect to the onset of IDC. The IDC regime has never been observed with absorbed powers below about 9 MW. The threshold electron density for IDC increased with increasing input power when the toroidal magnetic field was kept constant as seen in Fig. 9. The threshold value for $P_{abs} \sim 18$ MW of about $2.3 \times 10^{19} \text{ m}^{-3}$ agrees with a density level where the asymmetry in the particle recycling began to manifest as seen in Fig. 5. The threshold density decreased with increasing B_t . Lowering the toroidal magnetic field under 3.3 T led to excitation of frequent ELMs, which limited the electron density from rising higher than the threshold. This appears to be the cause for no IDC regime in low B_t discharges.

The I_p and B_t dependences of the threshold electron density appear to be summarized as a dependence on an effective safety factor q_{eff} [29]. Figure 11 indicates that the threshold electron density is approximately inversely proportional to the safety factor. It is important to note that the connection length of magnetic field lines around the main plasma increases with q_{eff} . These findings suggest that the IDC regime could be related to the connection length as well as ion ∇B drift direction.

4.2 Time evolution of IDC

The transition from L-mode confinement to the IDC regime was gradual and there were some time lags among various signals. The neutral pressure and oxygen impurity lines emitted from the main plasma dropped first at 4.7 s in Fig. 2. The rise rate of the plasma stored energy slightly changed around 5.2 s and the divertor radiation began to be enhanced at 5.4 s. The IDC regime was always preceded by an abrupt rise and fall of the O III (70.4 nm) signal along a vertical chord viewing the inside leg of divertor (U4) as seen in the bottom box at the right hand side of Fig. 2 (at 4.4 ~ 4.4 s). The electron density often did not increase during this phase. No appreciable change in edge T_e and n_e was observed by the Thomson scattering at the onset of IDC. The O II and O VI lines along the same chord and the O VI line along a slightly inner chord (Fig. 1b) behaved similarly to O III^{U4}. The O III lines were also measured by the 12-channel mirror-scanned monochromator. It was found that the farther the view from the X-point, the lower the O III brightness. Thus the O III^{U4} signal represents oxygen recycling from the divertor rather than charge-state changes of

oxygen ions. It should be noted that the neutral pressure and oxygen impurity lines never dropped when the heating power was less than 9 MW or the ion ∇B drift was away from the X-point. The O III^{U4} signal behaved similarly to the H $_{\alpha}$ ^{MAIN1} signal in this respect. Figure 12 shows the power dependences of the reduction in the oxygen line (O VIII and O III) intensities and a low-energy (~ 0.5 keV) charge-exchanged neutral flux from the main plasma in the case of the ion ∇B drift toward the X-point. The ordinate represents the ratio of the steady-state value to the peak one during each NBI pulse. The oxygen lines and the charge exchange flux are well correlated; they decrease during NBI pulse when the heating power is higher than 9 MW and the reduction is significant when the power is above 15 MW. The drop in the O III ratio is the most drastic. Such a reduction in any of the three signals was never been observed when the ion ∇B drift was away from the X-point.

Figure 13 illustrates the time evolution of the bolometer array signals in a typical IDC discharge shown in Fig. 14. There should have been density hesitation around 5 s if the NB power had been kept constant. The signal from a bolometer viewing the core plasma (channel 13) diminished in correlation with the reduction of the oxygen lines as shown in Fig. 14(a). Then the plasma stored energy started to rise. Although carbon impurity lines began to rise at this moment, the carbon emission intensity normalized to the electron density did not increase significantly during the improved phase. The C II emission and radiation power from the divertor region increased with a time lag of 0.05 \sim 0.4 s. The enhanced divertor radiation is considered to be caused by increased carbon influx from the divertor plates. The C II intensity is plotted as a function of the peak surface temperature of the inner divertor plates in Fig. 15(a). Although the data was taken with the

same IR camera as the data of Fig. 14, the field of view was nearer to the edge of tiles than that in Fig. 14. The C II intensity increases with rising temperature, in particular, above 900 K. The rise of the corresponding edge temperature at the leading edge of those tiles is estimated to be higher by a factor of $2 \sim 3$ based on a magnetic field pitch of about $1/40$ and a maximum gap between adjacent tiles of 1.5 mm for a 1-MA discharge. Thus radiation-enhanced sublimation [30] could be the dominant mechanism for the carbon influx rather than chemical sputtering, whose erosion maximum occurs slightly below 900 K [31]. By approximating the sputtering yield as $\Gamma_C / \Gamma_H \propto C II / H_\alpha$ and the increment of the leading edge temperature to be twice that of the surface temperature, one gets an Arrhenius plot as Fig. 15(b), which reveals a temperature independent physical sputtering yield at low temperatures and thermally activated sputtering yield above 1300 K. The estimated activation energy of about 1 eV (the slope of the solid line) agrees with the radiation-enhanced sublimation by hydrogen ions [30,31].

Eventually the discharge reached a quasi-steady state, which lasted until the NB power dropped below the threshold. Visible bremsstrahlung measurement indicated that Z_{eff} was $3 \sim 4$, slightly increasing during the improved phase. Thus, oxygen ions were exchanged for carbon ions. Note that no "carbon bloom" phenomenon which can cause deterioration of energy confinement [32-34] was observed even under 25-MW NB injection for 4 sec.

4.3 Global power balance

Global power balance was examined by evaluating the heat flux onto the divertor plates with the infrared camera. An example of time evolution of the measured peak temperature and evaluated power to the plates is shown in Fig. 14 (b) and (c). The maximum surface temperature of the plates did not exceed about 800°C within a 4-sec beam pulse. The peak heat flux was less than 5 MW/m² even under 22-MW heating and it dropped during the IDC regime. Figures 14(b) and 16 show that there was an asymmetry in the heat flux onto the divertor plates; the reduction of heat flux was larger at the inner separatrix (ion drift side) resulting in a decrease in the peak temperature of the inner divertor plates. The similar asymmetric behavior was observed in H α TV images of the plates. The hydrogen recycling at the inner separatrix increased during the early phases and it decreased during IDC, the signatures of which can be seen in the H α^U 4 trace of Fig. 2.

Although the missing power is not negligible in the early phase of NB heating, most of the input power is accounted for in the later phase as shown in Fig. 14(c). The total power load on the divertor plates during the IDC regime was estimated to be less than one third of the input power. The radiation power from the divertor region including the X-point increased up to nearly a half of the input power. The total radiation power from the main plasma was about a quarter of the input power in the beginning. It then declined to less than one fifth of the input power over the period from 5.5 to 6.3 sec (Fig. 14). During this same period, power to the divertor plates increased until the divertor radiation was significantly enhanced. Most of the power from the main

plasma at the later phase was radiated near the X-point with reduced radiation from the core plasma as seen from the change in the bolometer signal distribution in Fig. 13. Metal impurity densities have been low in divertor configurations with graphite tiles [19].

The parameter dependence of the divertor radiation is examined in Fig. 17: (a) A significant enhancement in the divertor radiation was observed when the absorbed power exceeded 15 MW; (b) irrespective of the absorbed power, the divertor radiation power increased at $\bar{n}_e \sim 3 \times 10^{19} \text{ m}^{-3}$ when no gas was puffed during NBI heating phase; (c) the increment in the divertor radiation was well correlated with the increment in the C II emissivity in the divertor region. These data are from 1-MA discharges with the ion ∇B drift toward the X-point including non-IDC phases. The toroidal magnetic field is constrained to be 4 ~ 4.5 T for (a) and (b) and 4.5 T for (c). Figure 17(d) shows that attainable divertor radiation power depended on the toroidal magnetic field; the higher magnetic field, the higher divertor radiation could be achieved. When B_t was less than 3 T, the ratio of the divertor radiation to the absorbed power remained less than 20%.

Whereas Ne gas was puffed into IDC plasmas, we could not increase the radiation power from the divertor region further. The carbon impurity influx decreased instead. Thus carbon ions in the divertor plasma were replaced by Ne ions. The Ne puff, however, could lower the threshold power for IDC to about 7 MW.

4.4 Energy confinement improvement by IDC

Figure 18 shows the plasma stored energy evaluated from the diamagnetic measurement as a function of the total absorbed power.

The ion ∇B drift direction is toward the X-point. The line averaged electron density is in the range of $(2 \sim 4) \times 10^{19} \text{ m}^{-3}$. The non-IDC data points which are shown as closed symbols obey an offset linear law. These data are from phases around the threshold density or gas puffed phases in which the transition into the IDC regime was delayed. The non-IDC data with the ion ∇B drift away from the X-point lie nearly the same line with slightly less incremental confinement time. The open symbols represent IDC data. The stored energy improved by up to 20% in the case of 1 MA and by up to 10% in the case of 1.5 MA discharges in going from non-IDC to IDC regimes. The energy confinement time, however, did not scale with I_p both in L-mode phase and IDC phase when the safety factor became less than three [35]. The data of 1.8 MA ($q_{\text{eff}} \sim 2.8$) and 2.0 MA ($q_{\text{eff}} \sim 2.6$) shots were not very different from that of 1.5 MA ($q_{\text{eff}} \sim 3.3$) shots. Although the improvement in energy confinement appears to be associated with the increase in electron density from time evolution of each shot, the energy confinement times collected from many shots did not depend on the electron density as seen in Fig. 19.

When a new set of data was taken in late 1989, the carbon influxes and resulting divertor radiation power for beam heated plasmas in later 1989 were not enhanced so much as in Fig. 17. The increment of C II was suppressed below two in the unit of Fig. 17(c) and the radiation power from the divertor remained less than 5 MW. However, the energy confinement still improved as shown in Fig. 18. To find the mechanism for this improvement, we examined correlations of the energy confinement time with several parameters. Some of the correlations are shown in Fig. 20. Here the energy confinement time is normalized to an absorbed power of 20 MW assuming a Goldston

scaling-like inverse-square dependence to cancel the power dependence of data from 14 MW to 22 MW. The improvement is best correlated with reduction in oxygen contents in the main plasma (a). The enhanced divertor radiation power appears to be a sufficient condition for the improvement rather than a necessary one (c). There is no correlation with carbon level (d). Although the neutral pressure data for the best improved data points are missing, the energy confinement improvement appears to be correlated with reduction in neutral pressure (b), namely improvement in particle confinement.

The electron temperature during IDC did not decrease with increasing density as seen in Fig. 14(a) in contrast to L-mode plasmas. Electron temperature profiles are compared in Fig. 21 to see the difference between IDC and non-IDC (ion ∇B drift down or up). The hatched area indicates the scatter in the Thomson scattering profiles obtained from about 10 shots. Data points near the center were missing because of the off-axis laser beam. Although the electron density profiles were almost the same within the scatter, the electron temperature was systematically higher during IDC with the ion ∇B drift toward the X-point. The profile shape did not change much during the IDC regime. The temperature and density profiles had shoulders near the edge presumably because of high magnetic shear near the separatrix. We could not exclude the possibility of central peaking of the profiles during IDC. Actually centrally peaked ion temperature profiles were sometimes observed by charge exchange recombination spectroscopy as illustrated in Fig. 22. This fact suggests that the IDC regime can be compatible with a hot-ion mode.

5. DISCUSSION

The IDC regime is a very interesting state where the remote radiative cooling is established with improved energy confinement. A large fraction of the heat flux to the divertor region was lost by radiation and charge exchange before it reached the divertor plates. Indeed most of the radiated power from the divertor plasma was accounted for by carbon and hydrogen emissions [8]. It is, however, very difficult to evaluate experimentally how much of the heat flux to the divertor is lost by charge exchange versus radiation. The large radiation power in the divertor region suggest that a cold and dense divertor plasma is formed during the IDC regime.

IDC is characterized by an improved particle confinement regime. To explain the improved particle confinement, there could be two possible scenarios: The divertor is more efficiently refueling the plasma, or the plasma has improved transport properties. The former is unlikely since the divertor H_α emission during IDC is lower than that during non-IDC (Fig. 6a) even when the hydrogen ionization rate is not different (Fig. 7a). The improved transport properties may be explained by Hinton and Staebler's theory [11]: the in-out asymmetry in the H_α emissivity at the divertor plates observed by the H_α TV camera agrees with the change in particle flux due to collisional transport near the separatrix [36]. The asymmetric particle recycling was confirmed by the vertical H_α measurement when the electron density exceeds the threshold for IDC as seen in Fig. 5. The in-out asymmetry was reversed with B_t reversal. The difference in the time evolution of H_α^{U4} and H_α^{DIV} signals came from the asymmetric particle recycling. The broken H_α^{DIV} trace in Fig. 2, which includes H_α emission at inner and outer strike

points of divertor, increased with electron density while H_{α}^{U4} , which is chiefly from the inner strike point, stayed constant. This implies that hydrogen particles recycled more at the outer separatrix (ion drift side) when the ion ∇B drift was away from the X-point. The in-out asymmetry in the particle recycling should pronounce the difference in $P_{NEUTRAL}^{MAIN}$ seen in Fig. 2 since the pressure was measured at the outer-side of the torus.

The positive feedback between particle confinement and divertor radiative cooling proposed by Staebler [12] is a plausible mechanism for the IDC phenomena. The radiated power from the divertor influences the temperature at the X-point and hence it enhances the collisional particle fluxes driven by electron temperature gradient. The buildup of carbon impurities responsible for the increase in divertor radiation in the inner divertor region agrees with the theory. However, refinement of the theory may be required to explain the time lag between the spontaneous change in particle confinement and the rise in divertor radiation.

Whereas the reduction of oxygen is correlated with the improvement in energy confinement, it is unlikely to be the direct cause. A clear correlation has been observed between oxygen concentrations and neutral pressures around the main plasma. The oxygen impurities appear to originate from walls due to the bombardment by charge-exchange particles, which is inferred from similar time evolution of oxygen line emissions and low-energy charge-exchange neutral fluxes. Indeed we have seen in Fig. 12 that those reductions due to NB heating are well correlated. The walls have been reported to be the main oxygen source through OH or H_2O formation [23, 37-39]. The oxygen appears to recycle at the divertor. The

improvement in energy confinement of up to 20% can not be explained by the decrement in oxygen impurities since the increment in the net heating power, i.e., heating power minus radiation power is only a few percent of the absorbed power in the core plasma.

The incremental energy confinement time for the data shown in Fig. 18 does not appreciably differ between IDC and non-IDC cases. This implies that the change in energy confinement is due to a change in 'background ohmic' confinement. The saturation of confinement improvement with plasma current when the safety factor is below three is common to divertor discharges in the L mode [35] and the H mode [25] although the mechanism has not been understood.

The gradual development and modest improvement in particle confinement are common to two regimes observed in ASDEX; IOC (improved ohmic confinement) [40] and counter NB injection [41]. However IDC is distinct from these regimes in respect that reduction of gas feed was not a prerequisite for transitions and that density peaking was not observed by Thomson scattering or interferometer measurements.

From the experimental observations, the time evolution of IDC may be described as follows:

- i) The particle confinement improves in discharges with the ion ∇B drift toward the X-point when the electron density reaches a threshold level which depends on heating power and the safety factor.
- ii) Oxygen impurities in the main plasma decrease owing to the reduced source by the decline in charge exchanged neutral particles which hit the walls. As a result, the radiation power from the main plasma falls.

- iii) The rate of temperature rise of the divertor plates increases with increased power to the divertor due to the reduced main plasma radiation. The carbon influx increases dramatically when the surface temperature exceeds 900 K.
- iv) Carbon impurities are accumulated in the divertor region by the enhanced divertor shielding effect. Accordingly, the divertor radiation power increases until the temperature rise of the plates becomes suppressed.
- v) The discharge reaches a quasi-steady state with the improved confinement and the enhanced remote radiative cooling.

The first step appears not to occur when the ion ∇B drift is away from the X-point. The IDC phenomena had never been observed in the outer X-point configuration of JT-60, either. These facts agree with the change in particle confinement due to collisional transport near the separatrix. Heating powers above the threshold for IDC may be required to steepen the temperature gradient along the field lines of SOL plasmas. The lower limit in the electron density which rises with increasing power may be imposed from the collisionality of the SOL plasma: Electrons must become collisional for the collisional effects to take place; $\nu_* = \nu_e R q / v_e > 1$, where ν_e , R , q and v_e are the electron collision frequency with ions, the major radius, the safety factor and the electron thermal speed, respectively. Since $\nu_e \propto n_e / T_e^{1.5}$, the condition of $\nu_* \sim 1$ leads to $n_e^{th} \propto T_e^2 / q$. From the Goldston type L-mode scaling, the plasma stored energy scales with $\sqrt{P_{abs}}$ and hence the volume averaged temperature rises as $\langle T \rangle \propto \sqrt{P_{abs}}$ for given density. Accordingly if one assumes $n_e^{SOL} \propto \bar{n}_e$ and $T_e^{SOL} \propto \langle T \rangle$, one gets $\bar{n}_e^{th} \propto P_{abs}/q$. This functional dependence agrees with the density threshold for IDC observed in Figs. 10 and 11. The collisional condition

of $v_* > 1$ for $T_e^{\text{SOL}} \sim 100$ eV and $Z_{\text{eff}} \sim 2$ plasmas with $R \sim 3$ m and $q \sim 4.5$ requires $n_e^{\text{SOL}} > 5 \times 10^{18} \text{ m}^{-3}$, which is about a quarter of \bar{n}_e^{th} . Since we do not have measurements of SOL plasma parameters, it is difficult to make a further quantitative argument.

We speculate that the connection length between the X-point and the divertor plates implicitly affect n_e^{SOL} and/or T_e^{SOL} . In this respect, it is of interest to note that a similar decrease in oxygen impurities occurred in beam heated limiter plasmas with circular cross-section resting on the inner bumper-type graphite limiters [19,41]. Vertical shift of the plasma opposite to the direction of the ion ∇B drift was found to prevent this oxygen reduction. Thus steps i) and ii) may occur even in limiter configuration with the limiters acting as heat sink.

The abrupt rise and fall of the O III^{U4} signal may indicate a change in the particle confinement. The global particle confinement time in beam heated plasmas degrades with power similarly to the energy confinement time [21]. The increase in O III^{U4} should reflect the enhanced particle recycling due to the drop in particle confinement with increasing density (see Appendix A) combined with the power degradation, which interpretation may be supported by the hesitation in electron density rise around the moment when the O III^{U4} signal reaches a peak. This density level coincides with the threshold for IDC. Then recycling particles begin to decrease due to the particle confinement improvement and hence resulting in the fall in O III^{U4} and the rise in density.

Step i) was initiated right after the NB injection when the electron density was above the threshold. At this early phase, the temperature of the divertor plates did not rise very much and hence the carbon influx remained at low levels. Thus steps iii) and iv) appear to be the

effect of the improved confinement rather than the cause. However, the enhanced divertor radiation which is due to the increased carbon influx contributes to maintaining or steepening the temperature gradient along field lines and hence to the continuity of the improved confinement phase. The carbon source is much higher in the case of the ion ∇B drift toward the X-point because the heat flux to divertor is higher due to the reduced radiation power from the main plasma compared to the opposite ion ∇B drift direction.

The radiation power density in the divertor plasma reached levels of up to 10 MW/m^3 during IDC. This is comparable to those in MARFE plasmas [43,44]. Thus, the IDC state can be viewed as an improved particle confinement regime with an associated MARFE radiation region located near the X point. The parameters of the divertor plasma in a weak IDC phase ($P_{\text{RAD}}^{\text{DIV}} \sim 4 \text{ MW}$) were estimated to be $T_e \sim 26 \text{ eV}$ and $n_e \sim 2 \times 10^{20} \text{ m}^{-3}$ with a carbon concentration of 0.3% [8]. Thus a cold and dense divertor plasma was realized. The carbon concentration in the divertor during more typical IDC phases is considered to be higher by more than three times this estimate. A dense divertor plasma might have been formed even before the IDC transition since high neutral compression, comparable to that in the outer semi-closed divertor [22], was realized; the neutral pressure measured by an RGA near the divertor (Fig. 1a) was 40 ~ 80 times larger than that at the lower outside port. In the presence of thermal neutrals, radiation from carbon impurities can be significantly enhanced by charge-exchange recombination [8,45,46]. Impurity charge-exchange processes with beam neutrals [47] may also partly contribute to the correlation between the oxygen concentration and radiation power from the main plasma.

The enhanced impurity shielding effects (Fig. 7b) which contribute to the buildup of carbon ions in the divertor plasma may be attributed to higher separatrix electron temperature away from the divertor compared to that in the reversed B_t direction. Carbon ions may accumulate near the X-point outside the high recycling region by thermal forces due to strong temperature gradient along the magnetic field [48]. However, we could not resolve carbon distributions in the divertor plasma within the diagnostics installed on JT-60.

The particle species dependence is central to discovering the mechanism for IDC. It is of interest to see whether the IDC phenomena would be realized in deuterium plasmas. There has been no report on IDC-like phenomena from JET or DIII-D. This is presumably because these machines have been operated at lower B_t field which is advantageous for H-mode transitions rather than IDC. Low B_t operation is disadvantageous for achieving remote radiative cooling as we saw in Fig. 17(d). The H mode often excludes IDC in two respects; ELM phases may restrict the density to rise higher than the threshold for IDC and ELM-free phases may reduce the power to the divertor due to the impurity enrichment in the main plasma. Experiments on JT-60U at $B_t = 4.2$ T [49,50] will reveal IDC characteristics in deuterium plasmas. As of September 1991, no IDC phenomena have been observed in JT-60U within the applied powers up to 21 MW at 4 T. Instead, ELM H phases were often triggered when heating power was above 12 MW.

6. SUMMARY

Prominent changes in light impurity behavior with B_t reversal were observed in the beam heated ($P_{abs} > 9$ MW) plasmas in the lower X-point configuration of JT-60. The IDC regime, improved particle confinement and remote radiative cooling, was achieved with ion drift toward the X-point. There was a threshold both in the electron density and input power. An improvement in energy confinement during IDC by up to 20 % was correlated with the improved particle confinement. The energy confinement time did not scale with plasma current and the improvement became less significant when the effective safety factor was below three. The decrease in oxygen impurities appears to be caused by the reduction in neutral particle density around the main plasma. The decrease in the radiation power from the main plasma resulted in increased power flux to the divertor. The surface temperature rise of divertor tiles above 900 K increased the carbon influx and hence the radiation power in the divertor. Eventually the quasi-steady state with remote radiative cooling up to a half of input power was established by confining carbon ions chiefly within the inner divertor separatrix. The in-out asymmetries in hydrogen recycling and carbon buildup agree with the collisional transport theory. No improvement in particle confinement nor enhanced divertor radiation were observed when the ion ∇B drift was away from the X-point. The hydrogen ionization in the divertor and impurity shielding effects were weaker than those with the ion ∇B drift towards the X-point.

ACKNOWLEDGEMENTS

The authors wish to thank the members of JAERI who have contributed to the JT-60 project throughout its progress. The authors also appreciate fruitful discussions with Drs. G.M. Staebler, L. de Kock, K. Itoh, S.I. Itoh and T. Takizuka.

References

- [1] SHIMOMURA, Y., KEILHACKER, M., LACKNER K., MURMANN, H., Nucl. Fusion **23** (1983) 869.
- [2] SENGOKU, S., SHIMADA, M., MIYA, M. et al., Nucl. Fusion **24** (1984) 415.
- [3] SHIMADA, M., NAGAMI, M., IOKI, K. et al., Nucl. Fusion **22** (1982) 643.
- [4] MULLER, E.R., BEHRINGER, K., NIEDERMEYER, H., Nucl. Fusion **22** (1982) 1651.
- [5] SHIMADA, M., WASHIZU, M., SENGOKU, S. et al., J. Nucl. Mater. **128** & **129** (1984) 340.
- [6] TSUJI, S., AKIBA, M., ANDO, T. et al., *Plasma Physics and Controlled Nuclear Fusion Research 1988* (Proc. 12th Int. Conf. Nice, 1988), IAEA, Vienna, Vol. 1, p. 265.
- [7] JT-60 TEAM, Plasma Phys. Controll. Fusion **31** (1989) 1597.
- [8] SHIMADA, M., KUBO, H., ITAMI, K. et al., J. Nucl. Mater. **176** & **177** (1990) 122.
- [9] TSUJI, S., NAKAMURA, H., YOSHIDA, H. et al., Kakuyugo Kenkyu **65** Supplement (1991) 243. (in Japanese)
- [10] NISHITANI, T., "Experimental Study of Radiation Losses on the JT-60 Tokamak", JAERI-M 90-087, Japan Atomic Energy Research Institute (1990), Sec. 5.2.
- [11] HINTON, F.L., STAEBLER G.M., Nucl. Fusion **29** (1989) 405.
- [12] STAEBLER G.M., Nucl. Fusion **30** (1990) 2295.
- [13] TERRY, J.L., MARMAR, E.S., CHEN, K.I., MOOS, H.W., Phys. Rev. Lett. **39** (1977) 1615.
- [14] BRAU, K., SUCKEWER, S., WONG, S.K., Nucl. Fusion **23** (1983) 1657.

- [15] SUCKEWER, S., HINNOV, E., SCHIVELL, J., "Rapid Scanning of Spectral Line Intensities in PLT Tokamak", PPPL-1430, Princeton Plasma Physics Laboratory (1978).
- [16] ITAMI, K., FUKUDA, T., IKEDA, Y. et al., J. Nucl. Mater. **176 & 177** (1990) 504.
- [17] NISHITANI, T., NAGASHIMA, K., SUGIYAMA, T. et al., Rev. Sci. Instrum. **59** (1988) 1866.
- [18] NISHITANI, T., ITAMI, K., NAGASHIMA, K. et al., Nucl. Fusion **30** (1990) 1095.
- [19] KUBO, H., SUGIE, T., SAKASAI, A. et al., Nucl. Fusion **29** (1989) 571.
- [20] YAMADA, K., TSUJI, S., SHIMIZU, K. et al., Nucl. Fusion **27** (1987) 1203.
- [21] TSUJI, S., JT-60 TEAM, in Controlled Fusion and Plasma Physics (Proc. 14th Europ. Conf. Madrid, 1987) Vol. 11D, Part I, European Physical Society (1987) 57.
- [22] NAKAMURA, H., ANDO, T., YOSHIDA, H. et al., Nucl. Fusion **28** (1988) 43.
- [23] BEHRINGER, K.H., J. Nucl. Mater. **145-147** (1987) 145.
- [24] STAMP, M.F., BEHRINGER, K.H., FORREST M.J., MORGAN, P.D., SUMMERS, H.P., J. Nucl. Mater. **162-164** (1989) 404.
- [25] BURRELL, K.H., ALLEN, S.L., BRAMSON, G. et al., Plasma Phys. Controll. Fusion **31** (1989) 1649.
- [26] NARDONE, C., BHATNAGAR, V.P., CAMPBELL, D. et al., in Controlled Fusion and Plasma Physics (Proc. 18th Europ. Conf. Berlin, 1991) Vol. 15C, Part I, European Physical Society (1991) 377.
- [27] NAKAMURA, H., TSUJI, S., NAGAMI, M. et al., Nucl. Fusion **30** (1990) 235.

- [28] NINOMIYA, H., YOSHINO, R., AKIBA, M. et al., *Plasma Physics and Controlled Nuclear Fusion Research 1988* (Proc. 12th Int. Conf. Nice, 1988), IAEA, Vienna, Vol. 1, p. 111.
- [29] STAMBAUGH, R.D., MOORE, R.W., BERNARD, L.C. et al., *Plasma Physics and Controlled Nuclear Fusion Research 1984* (Proc. 10th Int. Conf. London, 1984), IAEA, Vienna, Vol. 1, p. 217 .
- [30] ROTH, J., *Physics of Plasma-Wall Interactions in Controlled Fusion*, edited by D.E. Post and R. Behrisch, NATO ASI Series: Phys. Vol. **131**, Plenum Press (1986), p. 389.
- [31] ROTH, J., Nucl. Fusion, Special Issue (1984) 72.
- [32] ULRICKSON, M., THE JET TEAM, THE TFTR TEAM, J. Nucl. Mater. **176** & **177** (1990) 44.
- [33] REICHLE, R., SUMMERS, D.D.R., STAMP, M.F., J. Nucl. Mater. **176** & **177** (1990) 375.
- [34] STORK, D., CAMPBELL, D.J., CLEMENT, S. et al., in *Controlled Fusion and Plasma Physics* (Proc. 18th Europ. Conf. Berlin, 1991) Vol. 15C, Part I, European Physical Society (1991) 357.
- [35] NAITO, O., HOSOGANE, N., TSUJI, S. et al., Nucl. Fusion **30** (1990) 195.
- [36] ITAMI, K., in *Review of JT-60 Experimental Results from January to October, 1989*, JAERI-M 90-066, Japan Atomic Energy Research Institute (1990) p. 135.
- [37] POSPIESZCZYK, A., BAY, H.L., BOGEN, P. et al., J. Nucl. Mater. **145-147** (1987) 574.
- [38] WAELBROECK, F., ESSER, H.G., WINTER, J. et al., J. Nucl. Mater. **145-147** (1987) 665.
- [39] BEHRINGER, K., DENNE, B., MORGAN, P.D., STAMP, M.F., FORREST, M.J., J. Nucl. Mater. **162-164** (1989) 398.

- [40] SOLDNER, F.X., MULLER, E.R., WAGNER, F., et al., Phys. Rev. Lett. **61** (1988) 1105.
- [41] GEHRE, O., GRUBER, O., MURMANN, H.D. et al., Phys. Rev. Lett. **60** (1988) 1502.
- [42] NISHINO, N., KUBO, H, SAKASAI, A., et al. J. Nucl. Mater. **162-164** (1989) 386.
- [43] LIPSCHULTZ, B., LaBOMBARD, B., MARMAR, E.S. et al., Nucl. Fusion **24** (1984) 977.
- [44] LIPSCHULTZ, B., J. Nucl. Mater. **145-147** (1987) 15.
- [45] CAROLAN, P.G. PIOTROWICZ, V.A., Plasma Phys. **25** (1983) 1065.
- [46] ABRAMOV, V.A., KROTOVA, G.I., Sov. J. Plasma Phys. **13** (1987) 133.
- [47] PUIATTI, M.E., BRETON, C., DE MICHELIS, C., MATTIOLI, M., Plasma Phys. **23** (1981) 1075.
- [48] NEUHAUSER, J., SCHNEIDER, W., WUNDERLICH, R., LACKNER, K., Nucl. Fusion **24** (1984) 39.
- [49] HORIIKE, H., ANDO, T., HORIE, T. et al., in Proc. 13th Symp. on Fusion Engrg., Knoxville, 1989 (IEEE, 1990) Vol. 2, p. 1049.
- [50] NINOMIYA, H., ANDO, T., HORIE, T. et al., Plasma Devices and Operations **1** (1990) 43.
- [51] STANGEBY, P.C., McCracken, G.M., Nucl. Fusion **30** (1990) 1225.

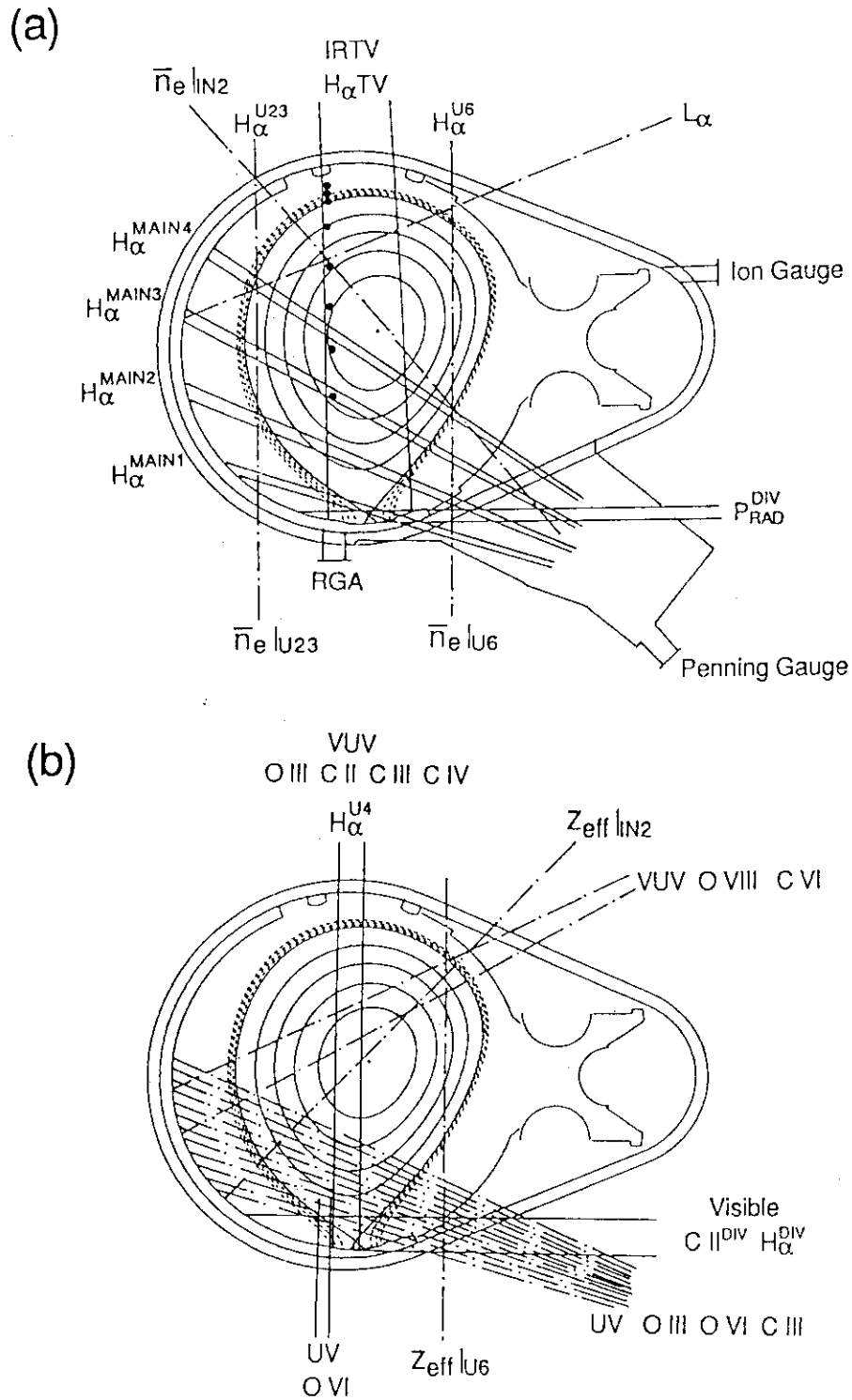


Fig. 1 Typical lower X-point configuration of JT-60 and location of diagnostics relevant to particle measurements and impurities. Solid lines and broken dot lines show the fields of view and center of chords, respectively. Thomson scattering measurement points are indicated by closed circles.

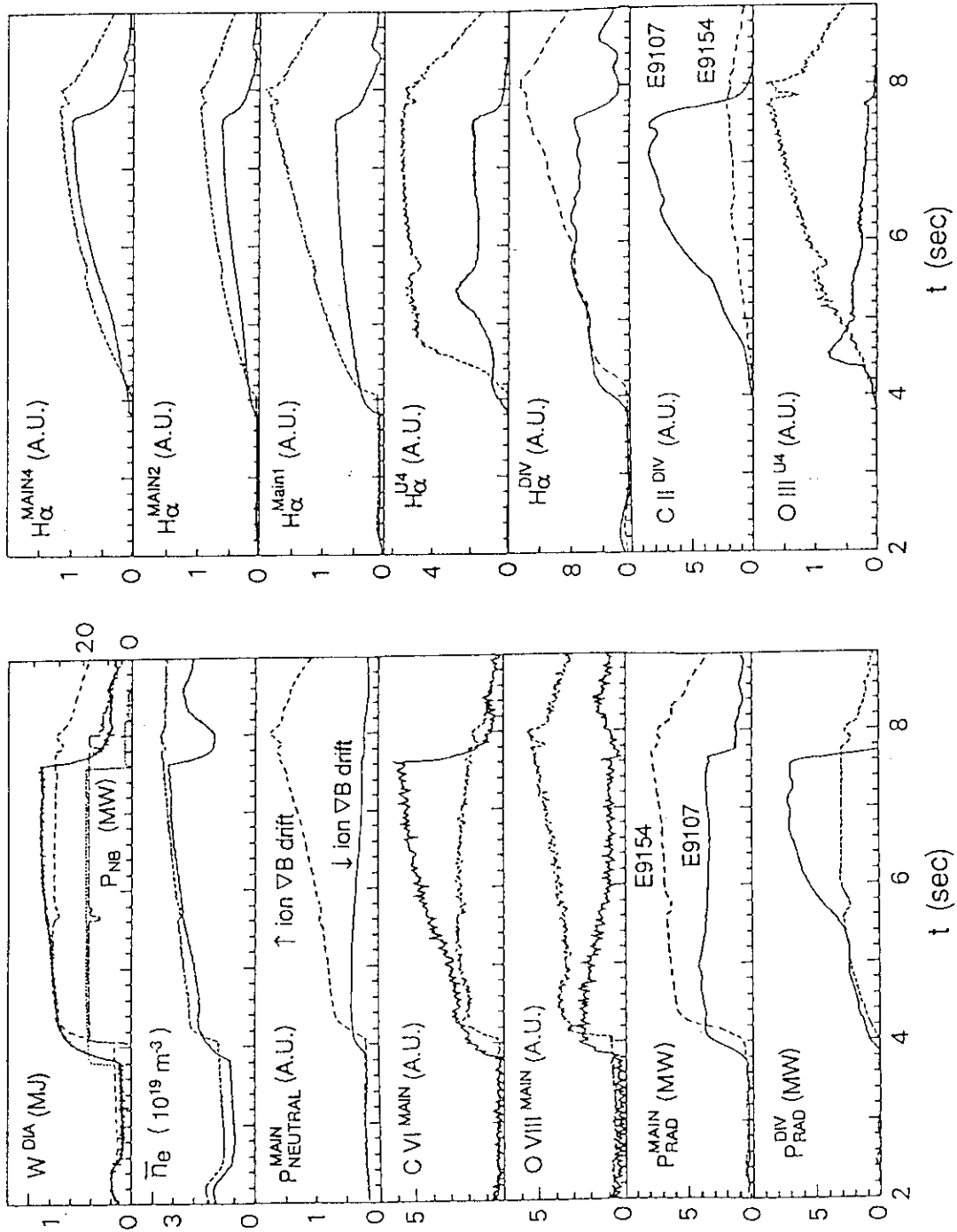


Fig. 2 Comparison of two discharges with nearly identical operational parameters except B_t and I_p polarities. Solid and broken lines show traces with the ion ∇B drift towards and away from the X-point, respectively. The H_α^{DIV} signal is free from C II line emission since it was measured by the visible spectrometer while the other H_α signals can be contaminated by C II line emission.

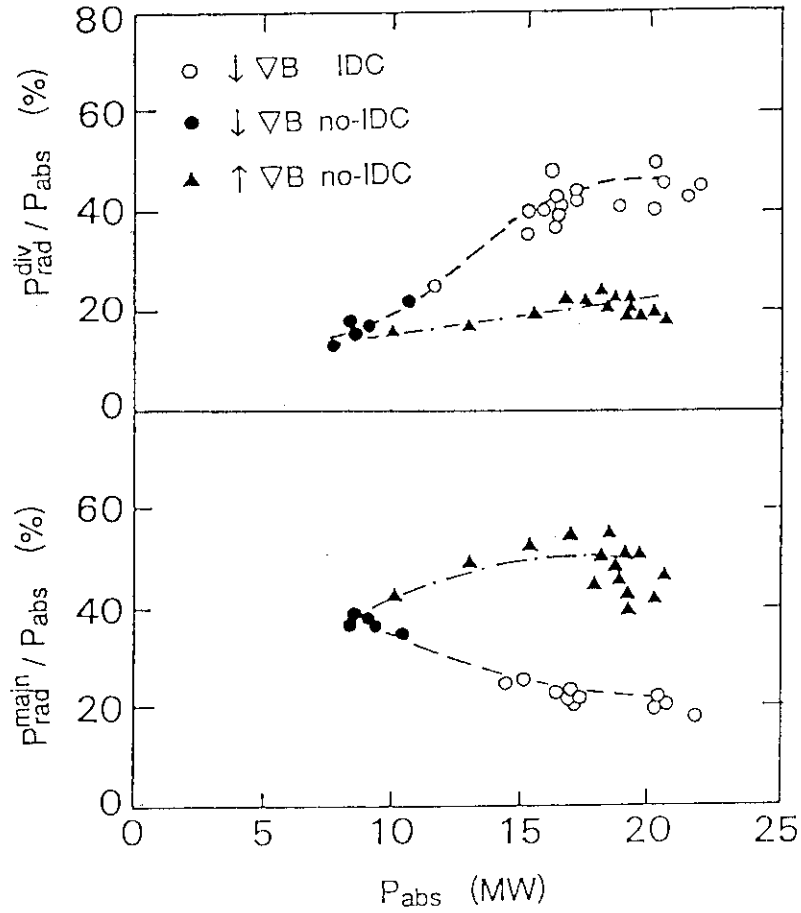


Fig. 3 Changes in radiation power fractions from the main plasma and divertor region with B_t reversal.

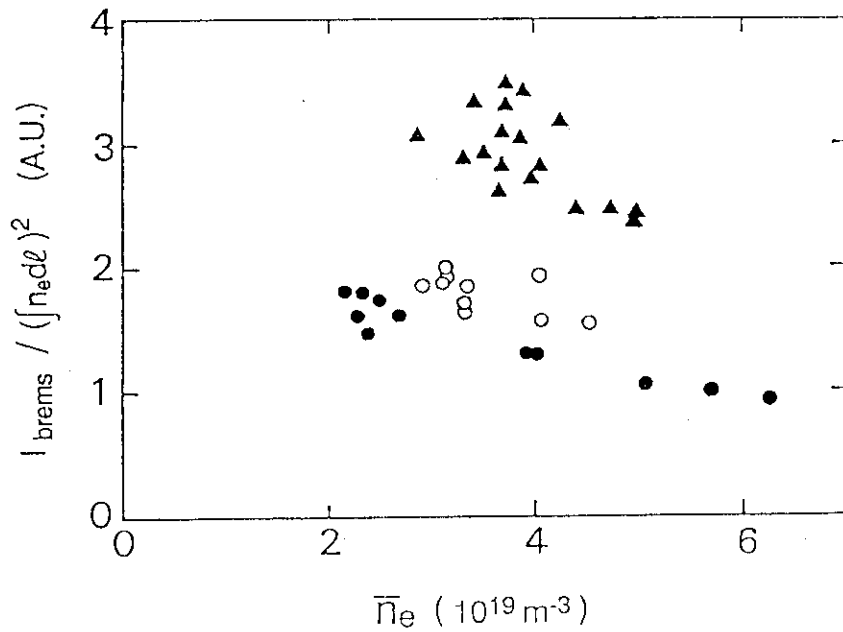


Fig. 4 Visible bremsstrahlung emission normalized to the square of the line electron density as a function of line averaged electron density. Symbols are the same as those in Fig. 3. The Z_{eff} values are higher with the ion ∇B drift away from the X-point.

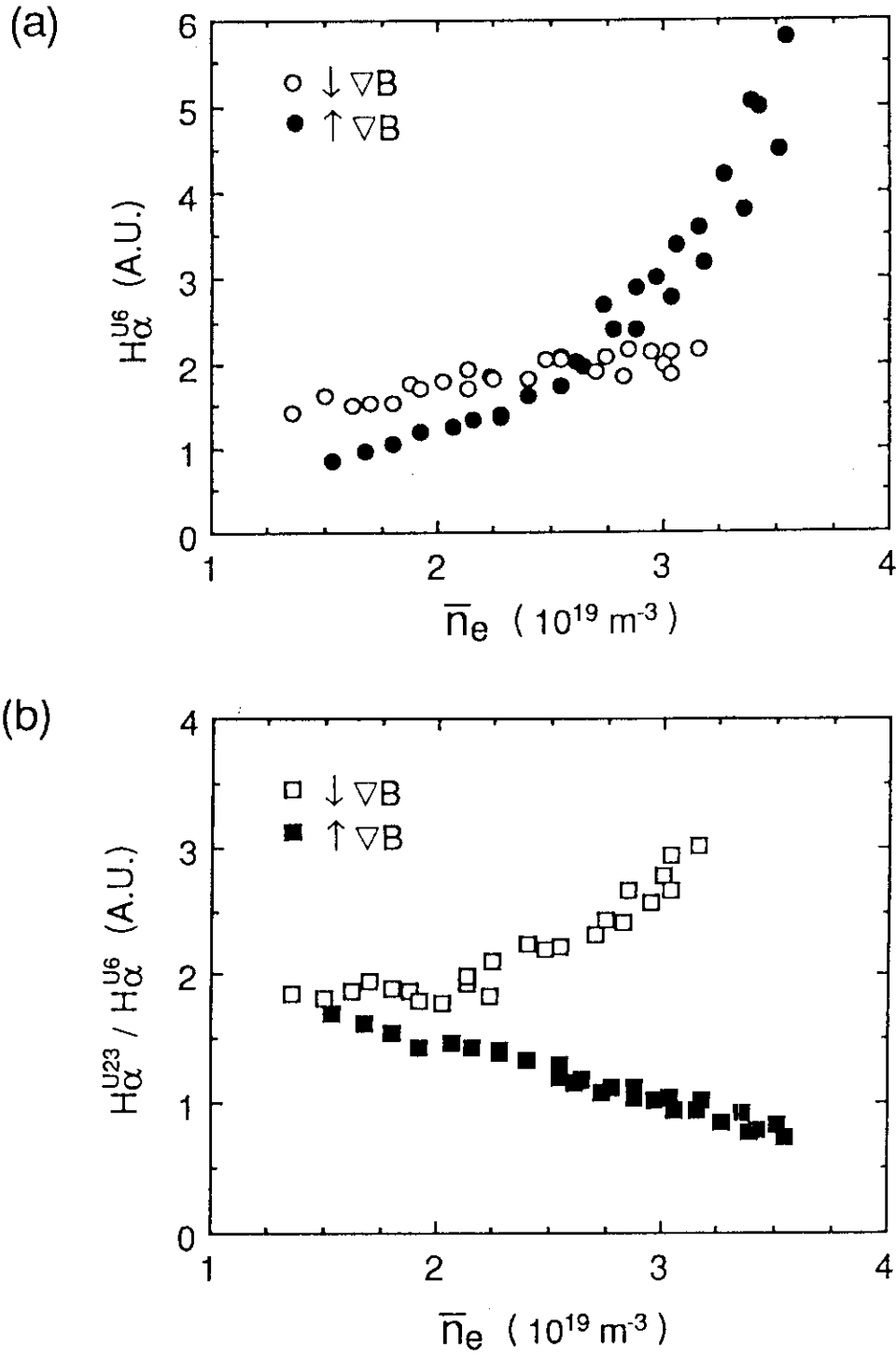


Fig. 5 Density dependences of the H_{α} emission along the outer vertical chord (a) and the ratio of inner (U23) to outer (U6) emission (b) when $I_p = 1 \text{ MA}$, $B_t = 4.5 \text{ T}$ and $P_{\text{abs}} \sim 18 \text{ MW}$. The ratio indicates that in-out asymmetry in particle recycling appears with increasing density and that its polarity changes with B_t reversal.

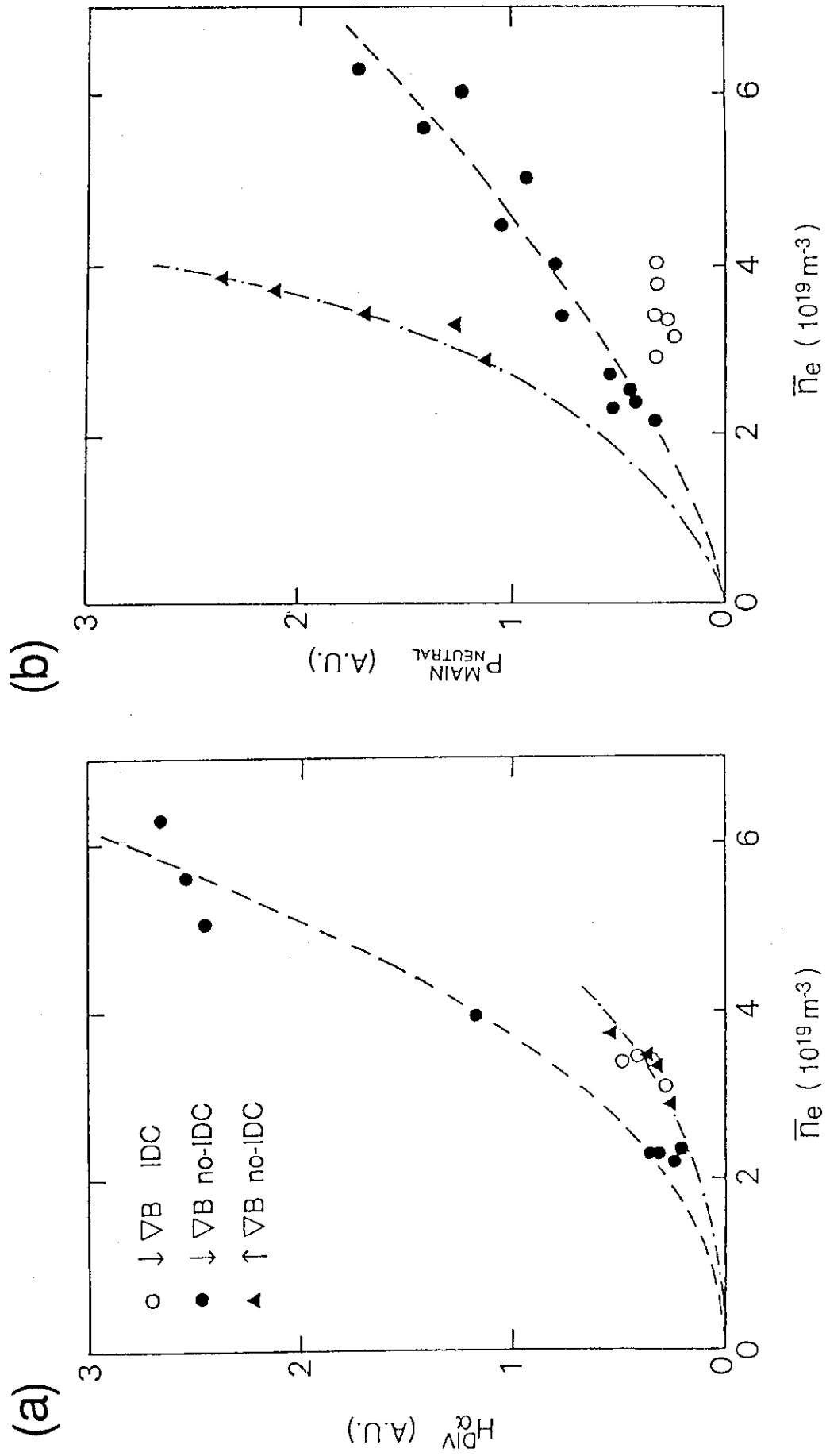


Fig. 6 Changes in particle recycling in the divertor region (a) and in neutral pressure around the main plasma (b) with B_t reversal.

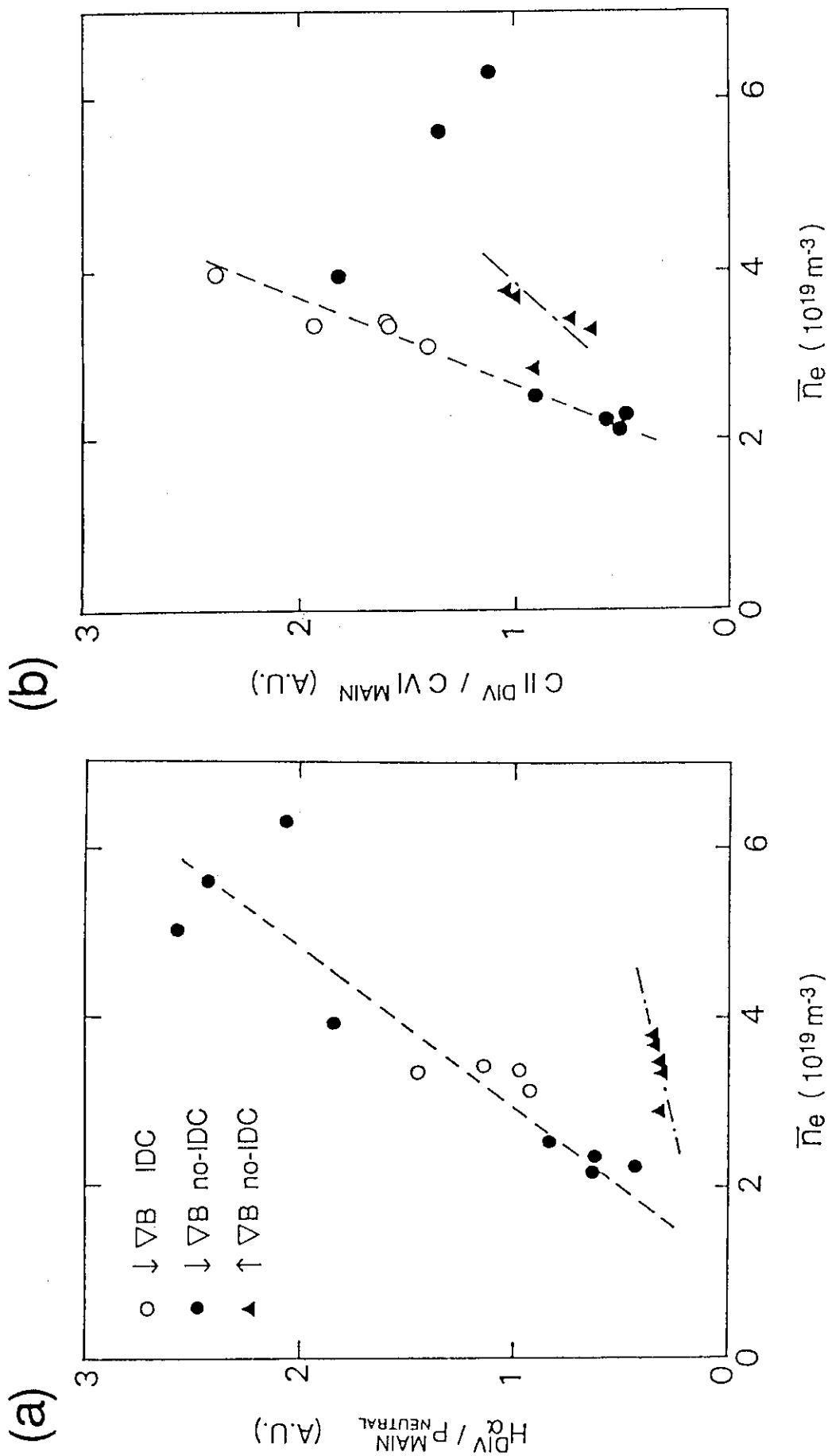


Fig. 7 Higher hydrogen ionization rate in the divertor region (a) and stronger shielding effect on carbon ions (b) with the ion ∇B drift toward the X-point. The IDC data points lie along nearly the same line as the non-IDC data. The two data points at higher density have lower carbon shield effects presumably because strong gas puffing cooled the SOL plasma.

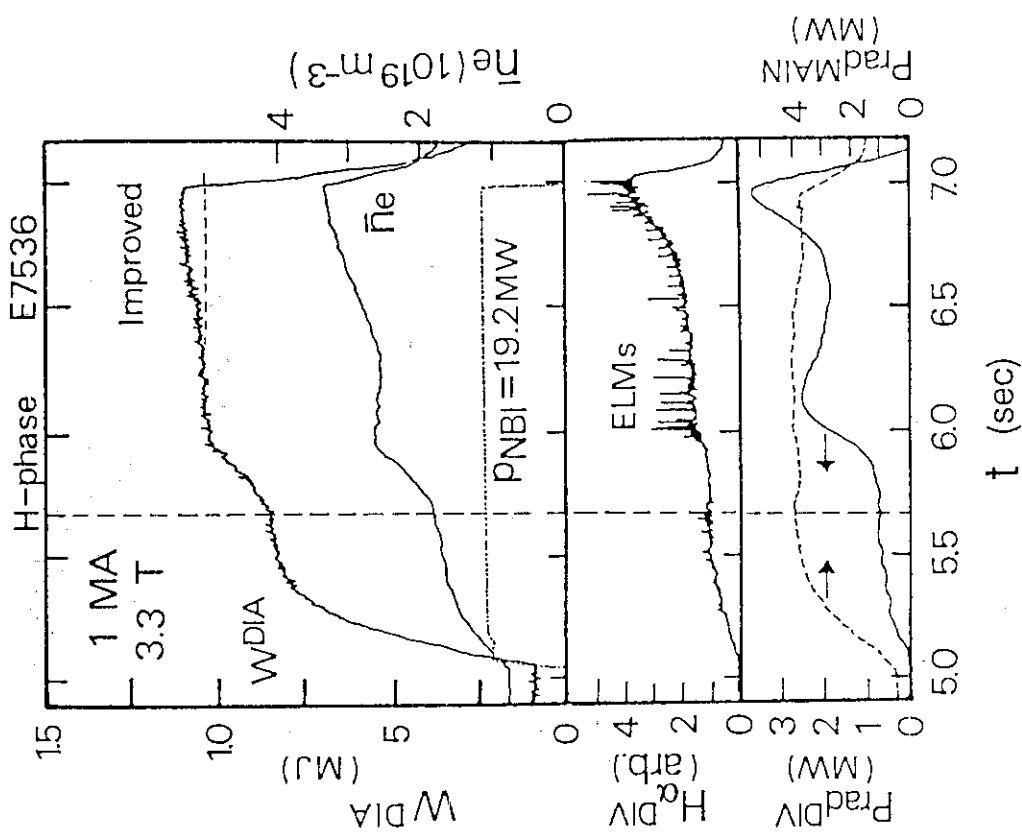


Fig. 8 Time evolution of a discharge where IDC was triggered in an ELMy phase of the H mode. Note that the divertor radiation increased with a delay from a spontaneous increase in the electron density. The H_{α}^{DIV} signal in this shot was contaminated by C II line emission.

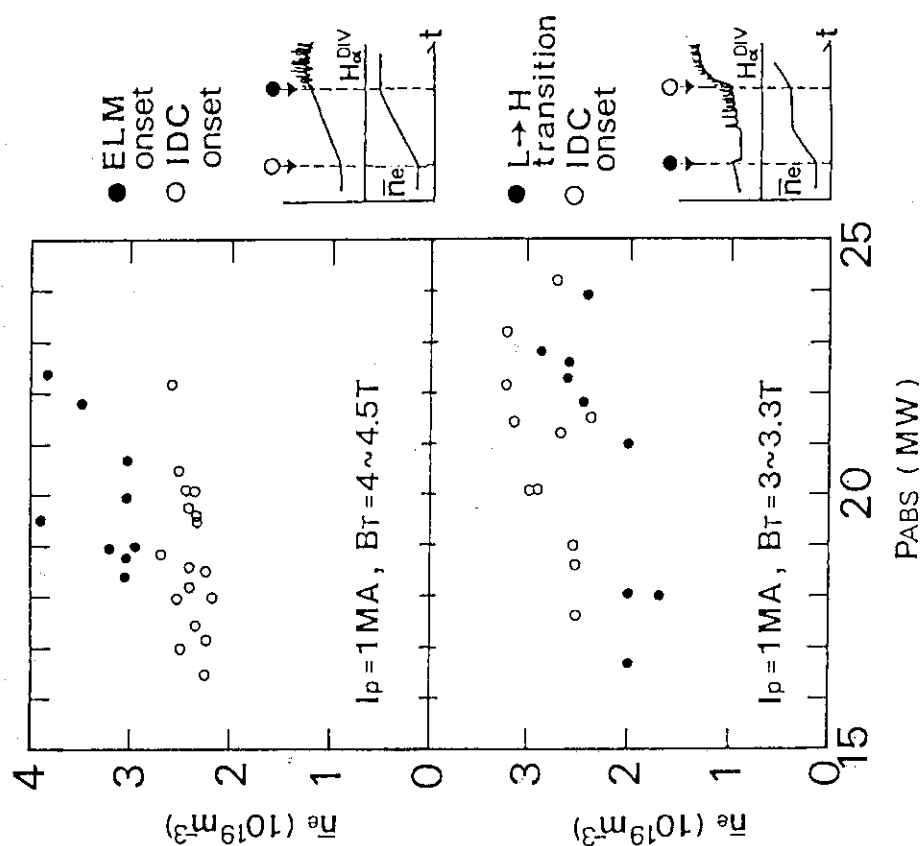


Fig. 9 Threshold electron densities of the IDC regime, H mode and ELMs as a function of absorbed power.

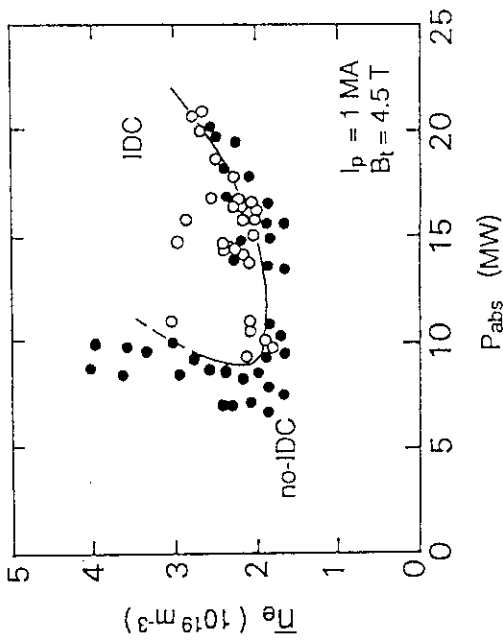


Fig. 10 IDC transition points (open circles) in terms of line averaged electron density and absorbed power. Closed circles represent that those discharges remained in the L mode.

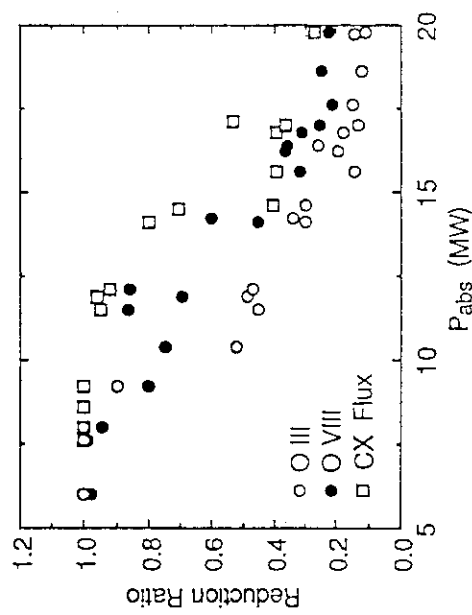


Fig. 12 Reductions in oxygen line emissions and a low-energy (~ 0.5 keV) charge exchange neutral flux with increasing power above a threshold of about 9 MW. The chord for the neutral flux is nearly the same as $H_{\alpha}^{\text{MAIN4}}$.

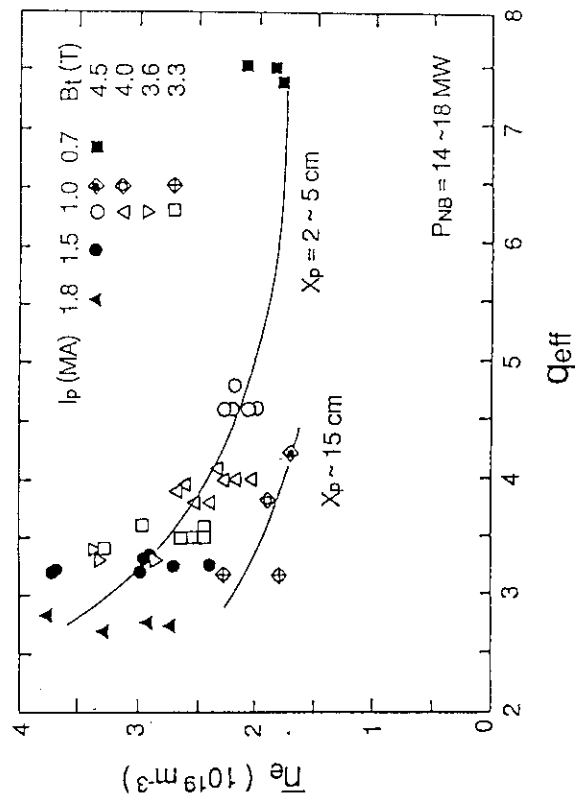


Fig. 11 Electron density threshold for IDC as a function of an effective safety factor. X_p stands for the height of the X-point above the divertor plates.

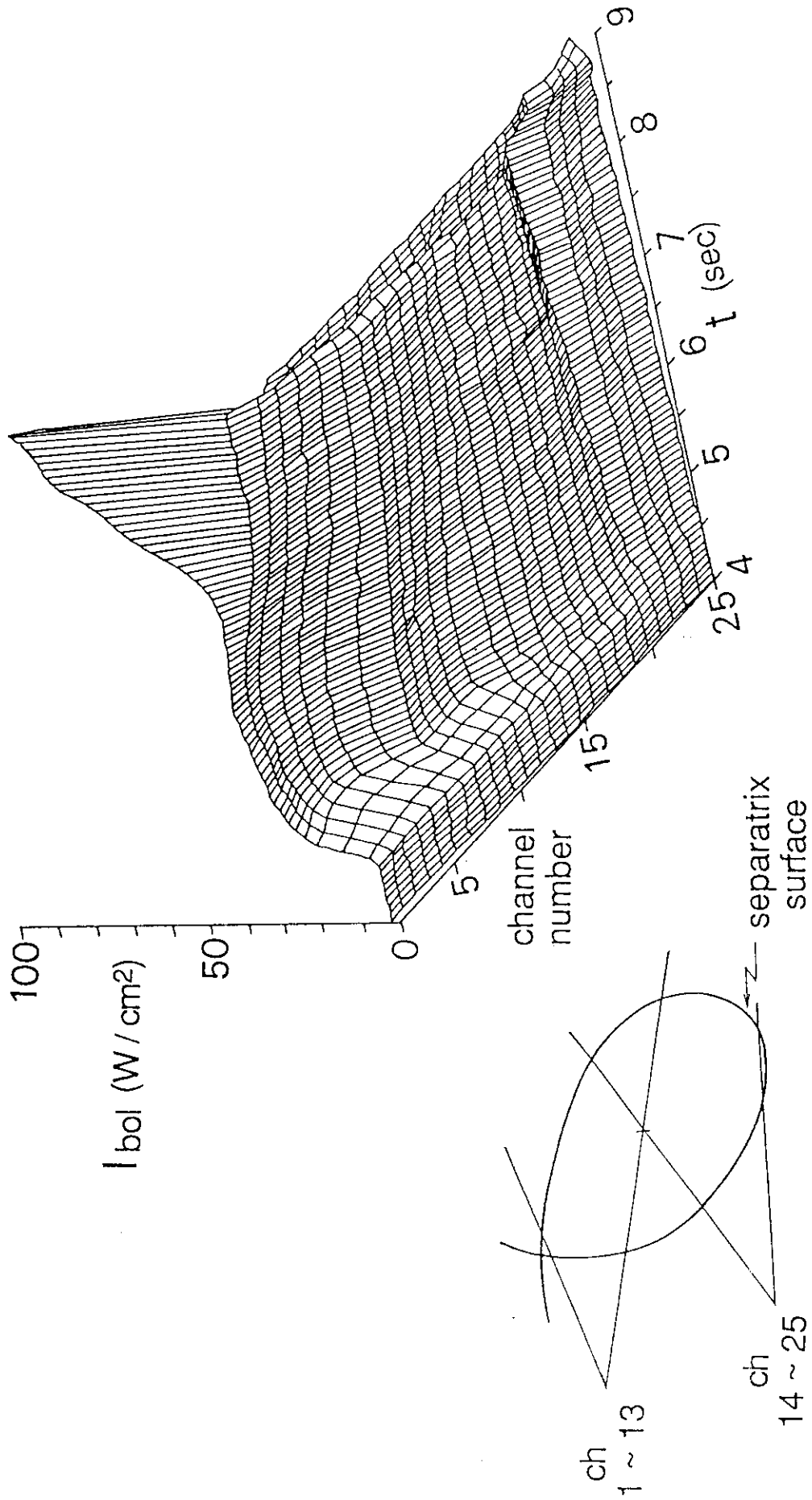


Fig. 13 Time evolution of bolometer signals in a shot in Fig. 14 which shows the localization of the radiation power near the X-point and a reduction in the core radiation with time.

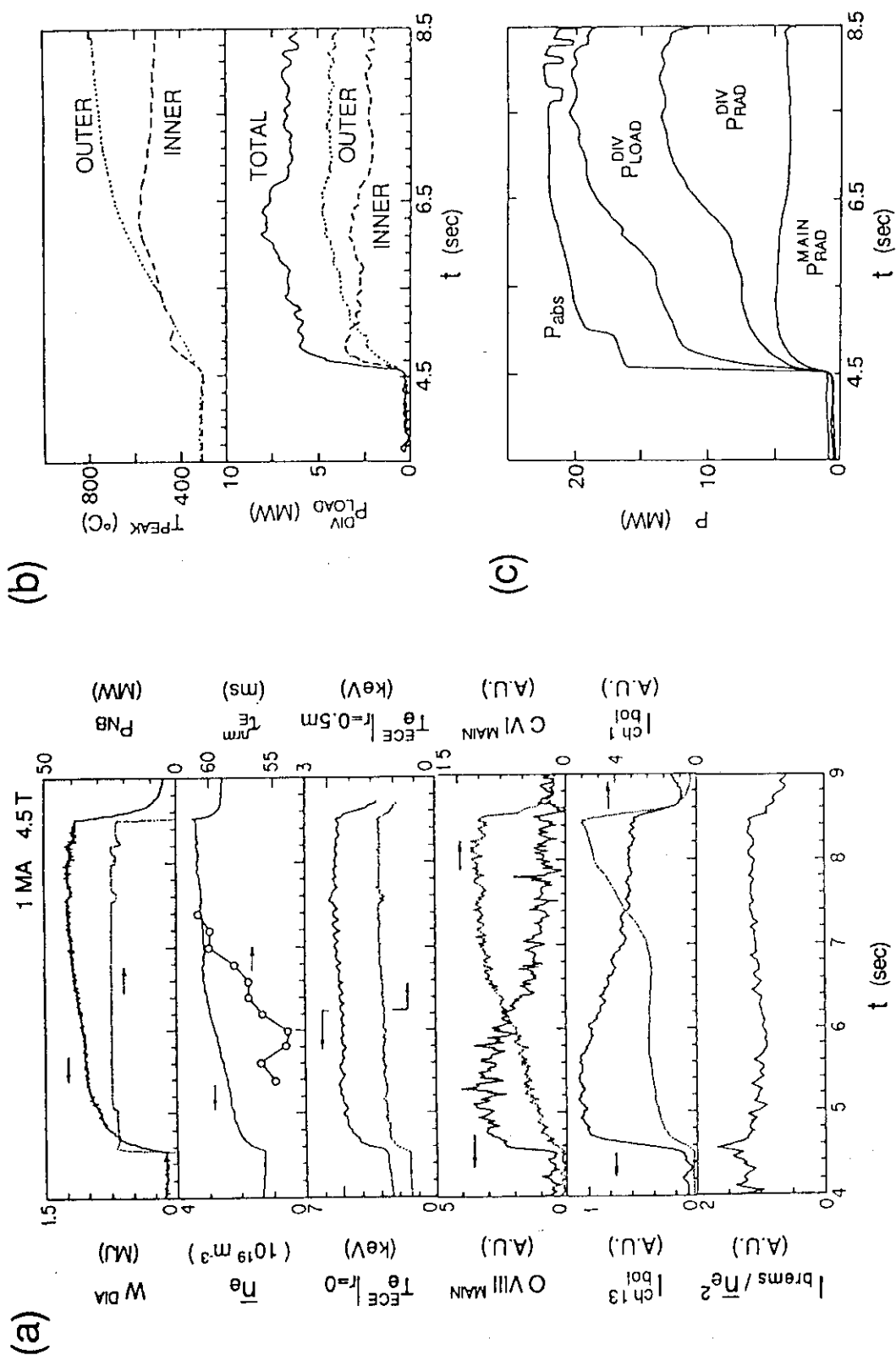


Fig. 14 Waveforms of a typical IDC discharge (a), time evolutions of peak surface temperatures of the divertor plates and power to the plates measured by IRTV (b) and power accountabilities (c). The energy confinement time is normalized one as in Fig. 19 to cancel an increase in the absorbed power. Two-channel traces from the bolometer array shown in Fig. 13 are displayed at the left hand side to see the correlation to other signals.

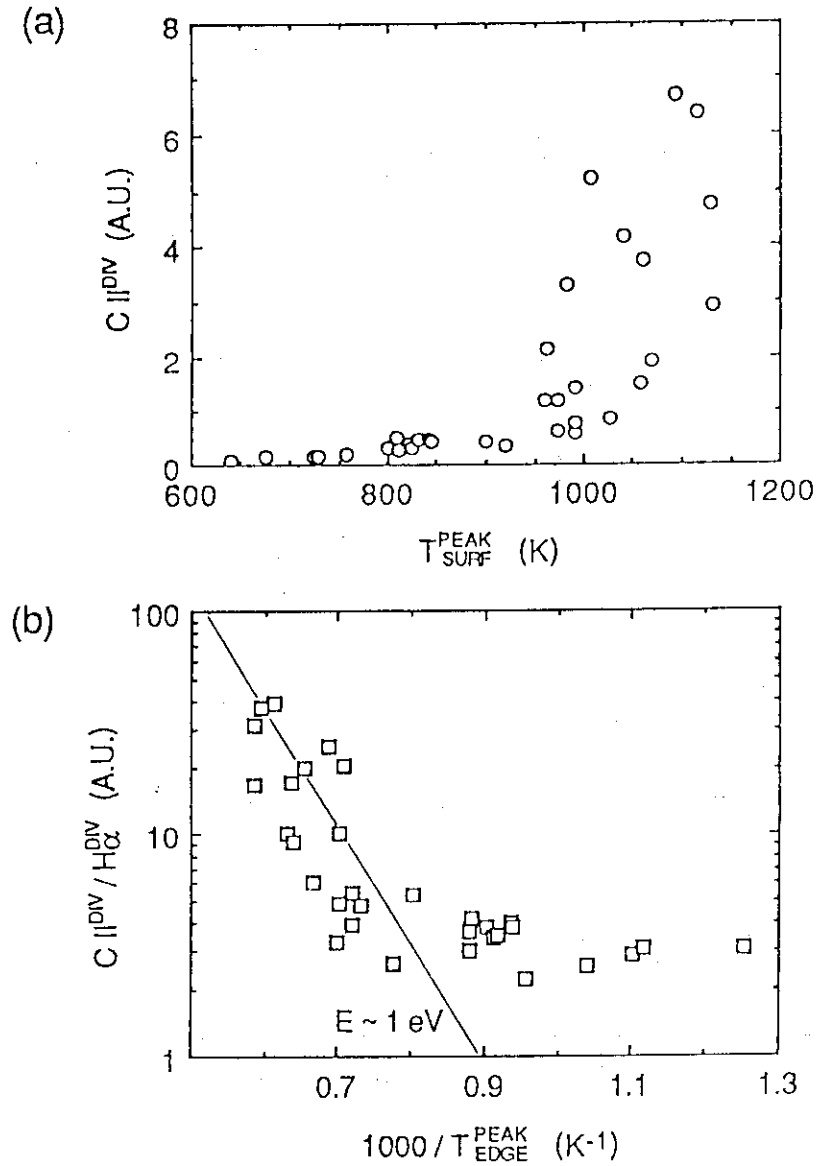


Fig. 15 (a) Temperature dependence of carbon influx from the divertor plates. (b) Arrhenius plot of an approximated sputtering yield. The solid line indicates a thermal activation energy of about 1 eV.

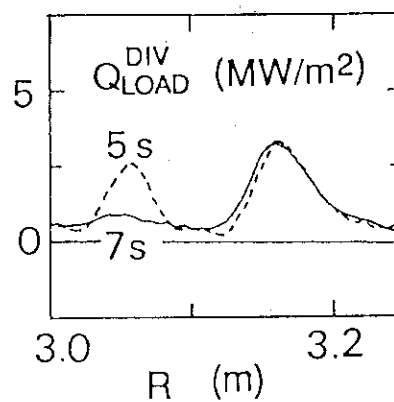


Fig. 16 Change in the distribution of power flux to the divertor plates before (5s) and during (7s) the IDC phase shown in Fig. 14.

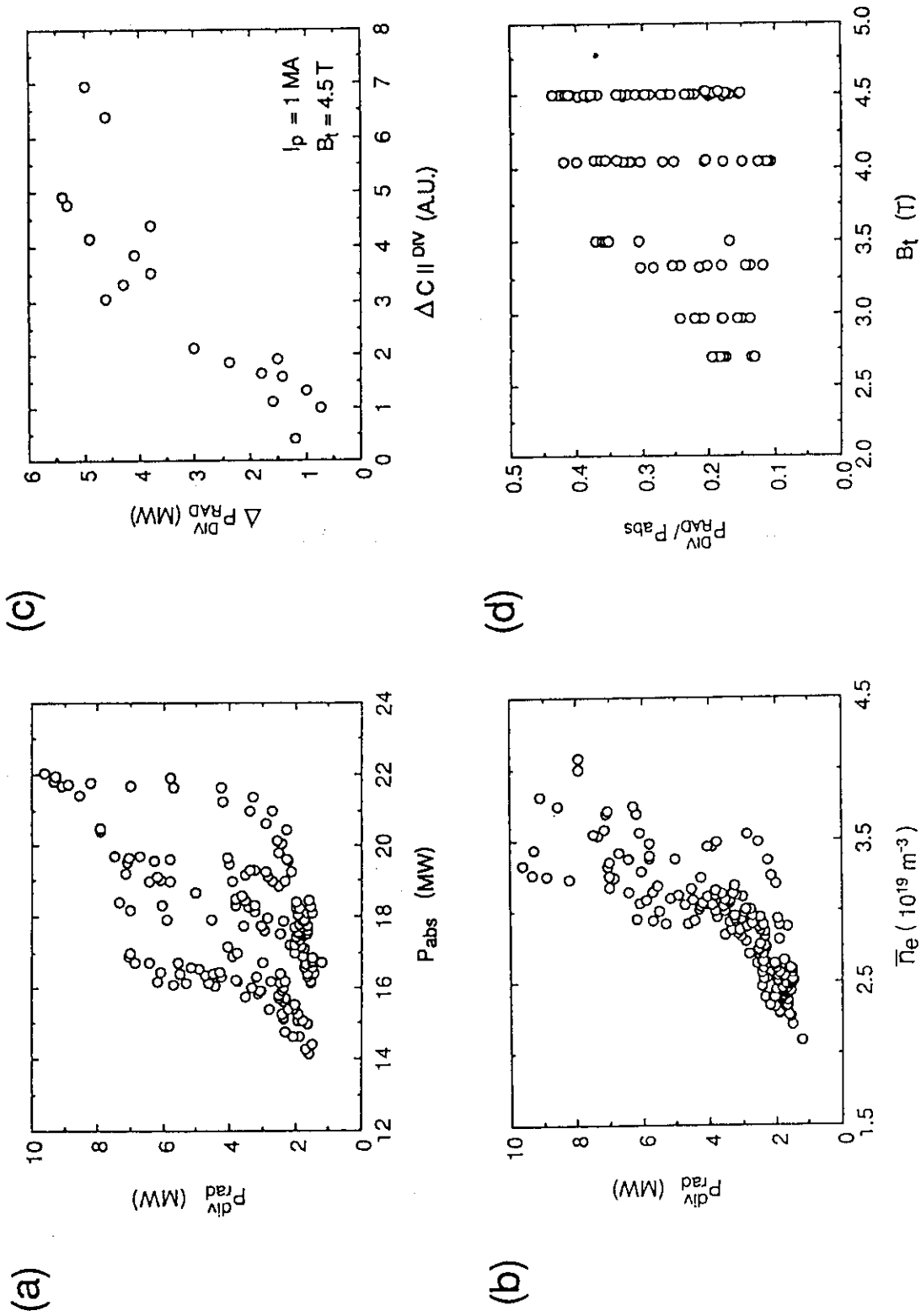


Fig. 17 Divertor radiation power dependences on heating power (a) and electron density (b) in the case of $I_p = 1 \text{ MA}$ and $B_t \geq 4 \text{ T}$. The increments in the radiation power are well correlated with those in the C II line emission (c). The ratio of divertor radiation to the heating power ($\bar{n}_e \geq 3 \times 10^{19} \text{ m}^{-3}$, $I_p = 1 \text{ MA}$) can be raised to higher levels with increasing toroidal magnetic field (d).

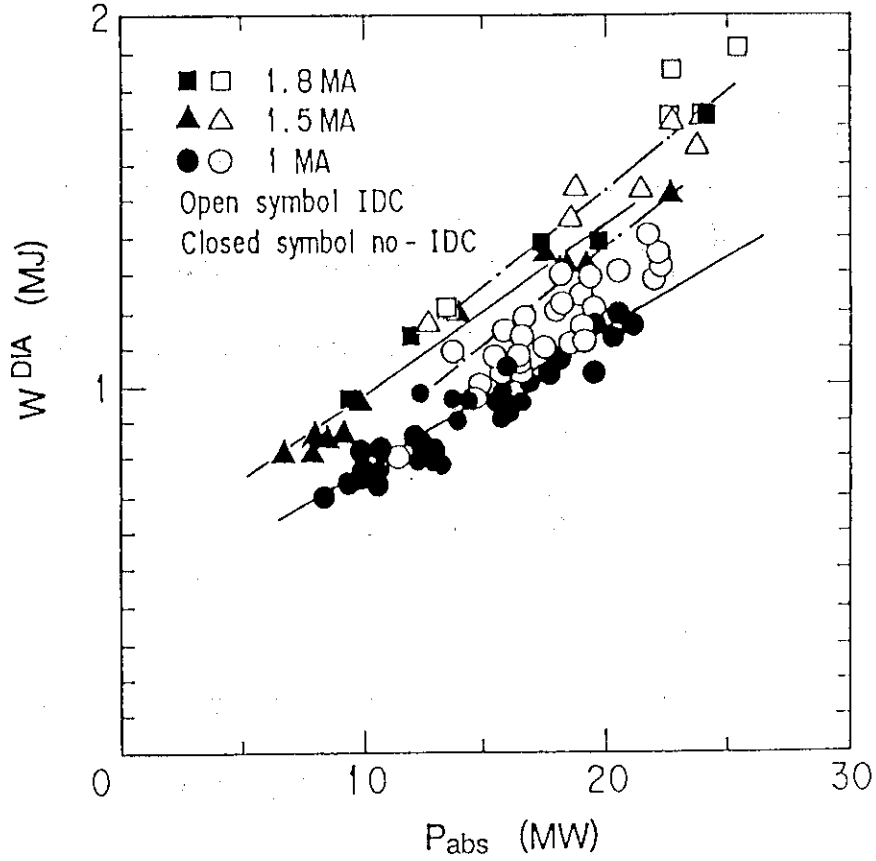


Fig. 18 The plasma stored energy as a function of absorbed heating power. The solid and broken dot lines represent an offset-linear dependence of the L mode and the maximum level achieved by IDC, respectively.

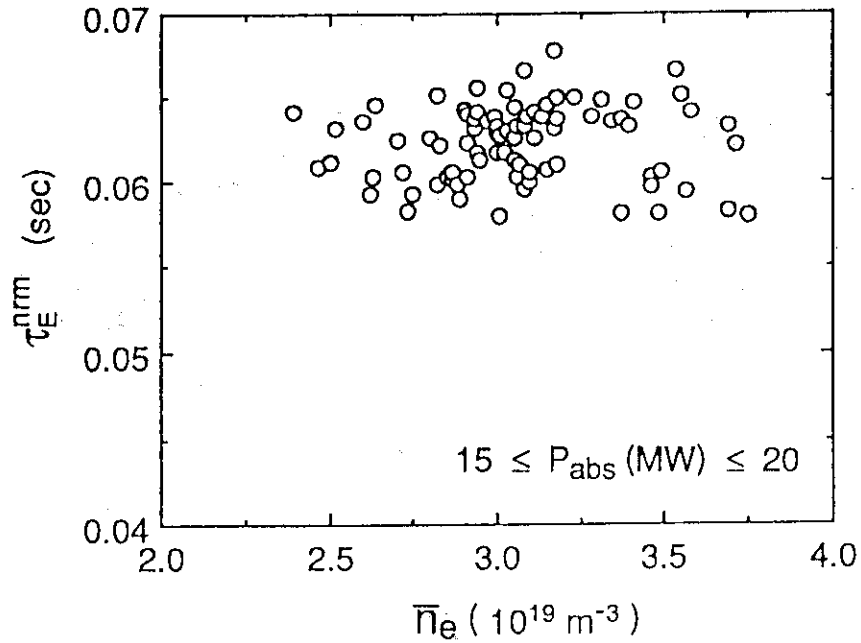


Fig. 19 No clear density dependence of the energy confinement time in the IDC regime. The absorbed powers from 14 MW to 22 MW are normalized to 20 MW by assuming inverse square power dependence of the energy confinement; $\tau_E^{\text{nm}} = \tau_E \sqrt{P_{\text{abs}}/20}$.

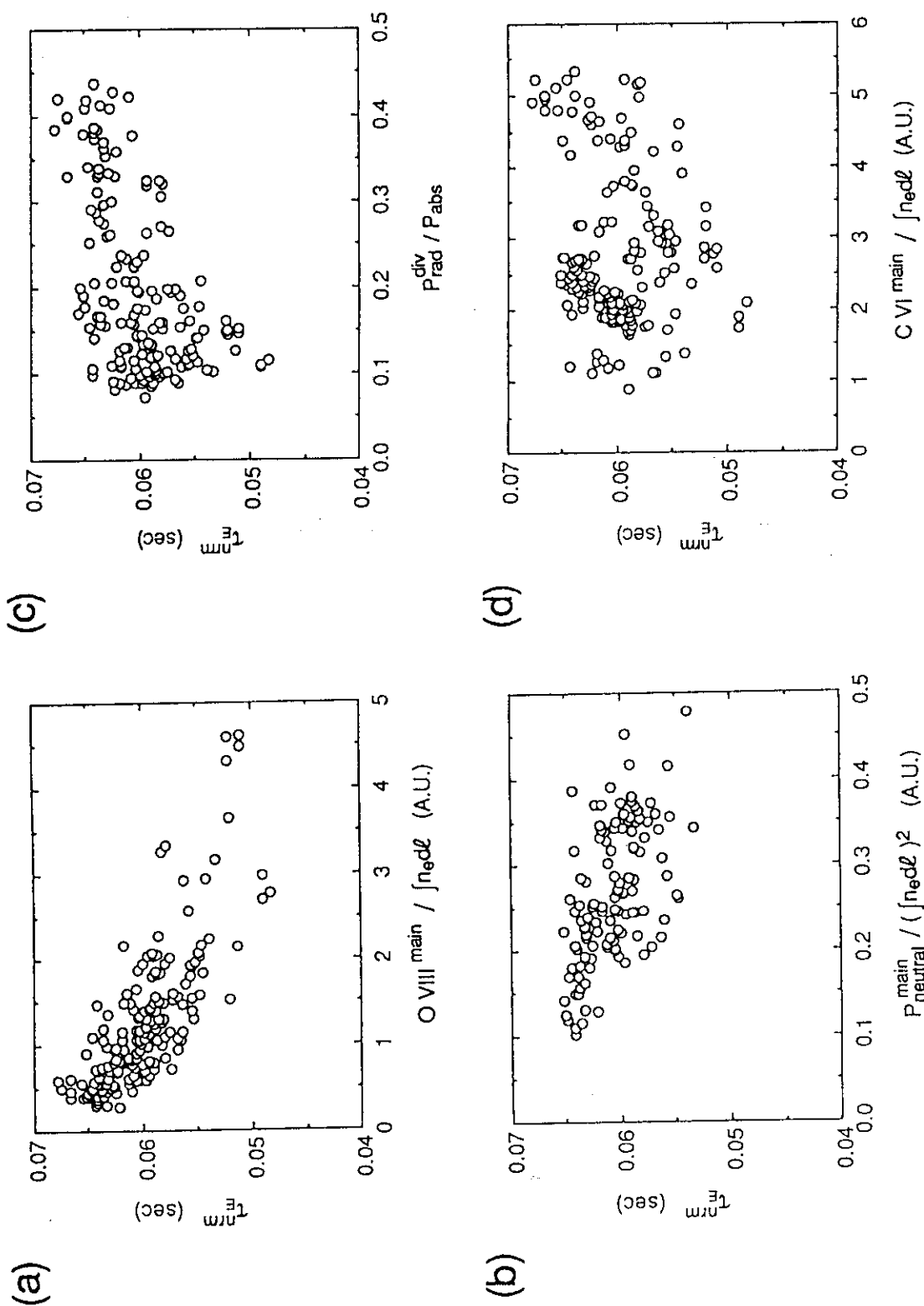


Fig. 20 Parameter dependences of the normalized energy confinement time on several parameters; oxygen contents in the main plasma (a), neutral pressure around the main plasma normalized to the square of the line density which is a measure of particle confinement degradation (b), divertor radiation power fraction (c) and carbon contents in the main plasma (d).

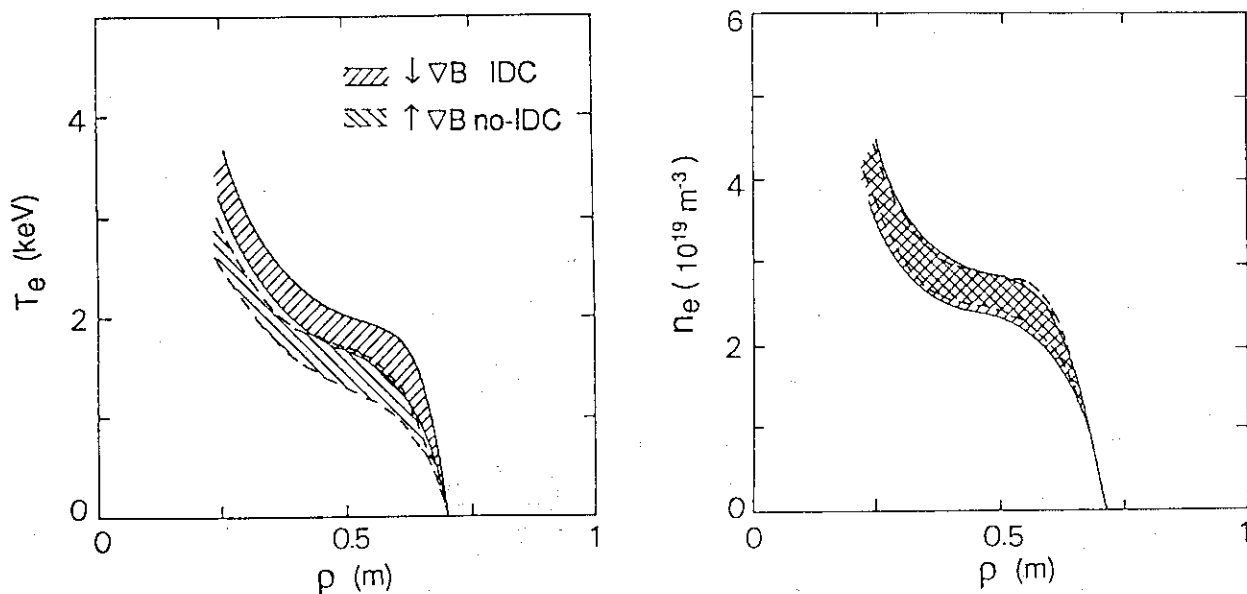


Fig. 21 Difference in the electron temperature profiles with B_t reversal. Hatched areas show the scatters in electron temperature and density profiles measured by Thomson scattering.

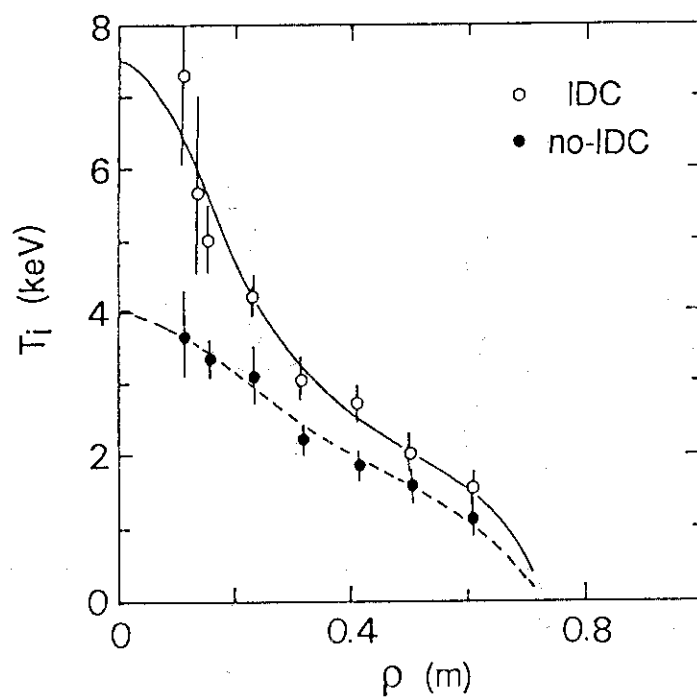


Fig. 22 The ion temperature profile obtained by charge exchange recombination spectroscopy at 5.8 sec (broken line) and 7sec (solid line) of the shot shown in Fig. 14.

APPENDIX A

Evaluation of Change in Particle Confinement from Electron Line Density and Neutral Pressure around the Main Plasma

The global particle confinement time is defined by the following equation,

$$\tau_p = \langle n \rangle V / \Phi_{in}^{main} \quad (1)$$

where $\langle n \rangle$, V and Φ_{in}^{main} are the volume averaged density, the plasma volume, the total neutral influx to the main plasma, respectively. The neutral influx can be expressed by Eq. (2) assuming a linear density profile within ionizing region $(a - \lambda_{iz}, a)$ in slab geometry [51]:

$$\Phi_{in}^{main} = D_{\perp} A_p n(a - \lambda_{iz}) / \lambda_{iz} \quad (2)$$

where D_{\perp} , A_p and $n(a - \lambda_{iz})$ are the cross-field diffusion coefficient, the plasma surface area and the plasma density at $r = a - \lambda_{iz}$. The ionization length is approximated as,

$$\lambda_{iz} \sim v_0 / 0.5 n(a - \lambda_{iz}) \langle \sigma v \rangle_{ion} \quad (3)$$

where v_0 and $\langle \sigma v \rangle_{ion}$ are the effective atom penetration velocity and the average ionization rate coefficient. Combining Eqs. (2) and (3) and assuming a similar density shape, $\langle n \rangle \propto \bar{n} \propto n(a - \lambda_{iz})$, we get the following two expressions:

$$\Phi_{in}^{main} \propto k \bar{n}^2 \quad (4)$$

$$\tau_p \propto V / k \bar{n} \quad (5)$$

where $k = \langle \sigma v \rangle_{ion} D_{\perp} A_p / 2 v_0$. The experimental observations of the parabolic dependence of recycling flux (the $H\alpha$ emission and neutral pressure) and inversely-linear dependence of the particle confinement time on density indicate that k is approximated to be constant. If one assumes that $\Phi_{in}^{main} \propto P_{H_2}^{main} = k' \bar{n}^2$,

$$\bar{n} \tau_p / V \propto 1/k \propto 1/k' = \bar{n}^2 / P_{H_2}^{main} \quad (6)$$

Therefore the right hand side of Eq. (6) is a measure of the improvement in the particle confinement.

APPENDIX B

Estimation of Divertor Ionization from Divertor $H\alpha$ Emission and Neutral Pressure around the Main Plasma

The strength of $H\alpha$ emission in the divertor region is proportional to the ionizing hydrogen particles,

$$\begin{aligned} I_{H\alpha}^{div} &= \int_{div} H\alpha \, dV \\ &\propto \int_{div} n_0 n_e \langle \sigma v \rangle_{ion} \, dV \\ &= \int_{div} \text{div} \Gamma \, dV = \Phi_{out}^{div} - \Phi_{in}^{div} \end{aligned} \quad (7)$$

where n_0 , Φ_{out}^{div} and Φ_{in}^{div} are the neutral density, the number of protons which reach the divertor plates and the number of protons which flow into the divertor region out of the main plasma,

respectively. If one assumes that the divertor plates are saturated with particles, the loss particles neutralized at the plates flow back to the upstream. The neutral pressure around the main plasma without gas-puffing should be proportional to the backflow particles which are not ionized by the divertor plasma. If one assumes that the neutral influx to the main plasma linearly increase with the neutral pressure as in Appendix A,

$$P_{H_2}^{main} \propto (1 - \eta_{ion}^{div}) \Phi_{out}^{div} \propto \Phi_{in}^{main} \quad (8)$$

where η_{ion}^{div} is a net ionizing coefficient in the divertor plasma. In steady state,

$$\Phi_{in}^{div} = \Phi_{out}^{main} = \Phi_{in}^{main} \quad (9)$$

Hence,

$$\begin{aligned} I_{H\alpha}^{div} / P_{H_2}^{main} &\propto (\Phi_{out}^{div} - \Phi_{in}^{div}) / \Phi_{in}^{main} \\ &\propto 1 / (1 - \eta_{ion}^{div}) - 1 \\ &= \eta_{ion}^{div} / (1 - \eta_{ion}^{div}) \end{aligned} \quad (10)$$

Since the right hand side of Eq. (10) is a monotonically increasing function of η_{ion}^{div} , large values of $I_{H\alpha}^{div} / P_{H_2}^{main}$ imply that ionization events in the divertor occur more efficiently.